*Astronomy & Astrophysics* manuscript no. output
October 9, 2020


# Physical characterization of S169: a prototypical IR bubble associated with the massive star forming region IRAS 12326-6245

N. U. Duronea⋆[1], S. Cichowolski⋆[2], L. Bronfman[3], E. Mendoza[4], R. Finger[3], L. A. Suad⋆[2], M. Corti⋆[1,5], and E. M. Reynoso⋆[2]

[1] Instituto Argentino de Radioastronomía (CCT-La Plata, CONICET; CICPBA; UNLP), C.C. No. 5, 1894,Villa Elisa, Argentina
e-mail: duronea@iar.unlp.edu.ar
[2] Instituto de Astronomía y Física del Espacio (UBA, CONICET), CC 67, Suc. 28, 1428 Buenos Aires, Argentina
[3] Departamento de Astronomía, Universidad de Chile, Casilla 36, Santiago de Chile
[4] Observatório do Valongo, Universidade Federal do Rio de Janeiro, Ladeira Pedro Antônio, 43, Rio de Janeiro - RJ, 20080-090, Brazil
[5] Facultad de Ciencias Astronómicas y Geofísicas, Universidad Nacional de La Plata, Paseo del Bosque s/n, 1900 La Plata, Argentina

Received ++++++; accepted ++++++

**ABSTRACT**

*Context.*
*Aims.* With the aim of studying the physical properties of Galactic IR bubbles and to explore their impact in massive star formation, we present here a study of the dust bubble S169, which is associated with the massive star forming region IRAS 12326-6245.
*Methods.* To study the properties of the molecular gas in the nebula and the IRAS source we used CO(2-1),$^{13}$CO(2-1), C$^{18}$O(2-1), HCN(3-2), and HCO$^+$(3-2) line data obtained with the APEX telescope using the on-the-fly full-sampling technique. To analyze the properties and distribution of the dust, we made use of images obtained from the IRAC-GLIMPSE, *Herschel*, and ATLASGAL archives. The properties of the ionized gas in the nebula were studied using radio continuum and H$\alpha$ images obtained from the SUMSS survey and SuperCOSMOS database, repectively. To search for stellar and protostellar objects in the region we used point source calalogues obtained from the MSX, WISE, GLIMPSE, 2MASS, AAVSO, ASCC-2.5V3, and GAIA databases.
*Results.* The new APEX observations allowed us to identify three molecular components, each one associated with different regions of the nebula, at −39 km s$^{-1}$(Component A), −25 km s$^{-1}$(Component B), and −17 km s$^{-1}$(Component C). Component A is the most dense and clumpy. Six molecular condensations (MC1 to MC6) were identified in this component, with MC3 (the densest and more massive one) being the molecular counterpart of IRAS 12326-6245. For this source, we derived an $H_2$ column density of about $8{\times}10^{23}$ cm$^{-2}$. An LTE analysis of the molecular emission on this source indicates a two-temperature regime (∼ 50 and 150 K) which is indicative of a central hot core and a cold enevelope. To explain the morphology and velocity of Components A, B, and C we propose a simple model consisting in a partially complete semi sphere-like structure expanding at ∼ 12 km s$^{-1}$. The introduction of this model led to a discussion about the distance to both S169 and IRAS 12326-6245, which was estimated to be ∼ 2 kpc. Several candidate YSOs were identified projected mostly onto the molecular condensations MC3, MC4, and MC5, which indicates that the star formation process is very active at the borders of the nebula. A comparison between observable and modeled parameters was not enough to discern whether the collect-and-collapse mechanism is acting at the edge of S169. However, other processes like radiative driven implosion may be acting at the borders of the nebula.

**Key words.** ISM: molecules, ISM: IR dust bubbles, ISM: individual object: S169, ISM:individual object: IRAS 12326-6245 .

## 1. Introduction

Massive stars modify the interstellar medium (ISM) where they are born through their stellar winds and UV photons, creating interstellar bubbles and HII regions. These nebulae are detected in the optical and radio continuum ranges, showing the presence of ionized gas, and at infrared (IR), millimeter, and sub-millimeter wavelengths, indicating both the presence of dust (at different temperatures) and molecules.

Milky Way surveys at IR wavelengths have provided a plethora of examples of bubbles/HII regions where their physical properties can be obtained on pc/sub-pc scales. Making use of the 8.0 $\mu$m *Spitzer*-GLIMPSE survey Benjamin et al. (2003a) Churchwell et al. (2006, 2007) identified more than 600 candidates for interstellar IR dust bubbles between Galactic longitudes of −60° to 60°. Follow-up observations of the stellar and pre-stellar populations around some of these bubbles have begun to link them with sites of recent triggered massive star formation (e.g. Zavagno et al. 2006; Watson et al. 2008; Deharveng et al. 2008, 2009; Samal et al. 2014; Kendrew et al. 2016; Duronea et al. 2017). This kind of studies provides important insights into the evolution of interstellar bubbles, the characteristics of the interstellar medium where they evolve, the role of massive stars on favouring or suppressing new generations of stars, and the physical conditions under which massive stars may be induced to form. As part of a project aimed at characterizing and studying the physical properties of Galactic IR bubbles and their surroundings, and to better understand their influence in massive star formation, we have selected a southern field containing the IR dust bubble S169 (Churchwell et al. 2006). The bubble is about 8 arcmin in diameter and is centered at RA, Dec. (J2000)= ($12^h35^m29\overset{s}{.}2$, $-62°58'03\overset{''}{.}8$). Fig. 1 shows a composite image

⋆ Member of the Carrera del Investigador Científico of CONICET, Argentina.

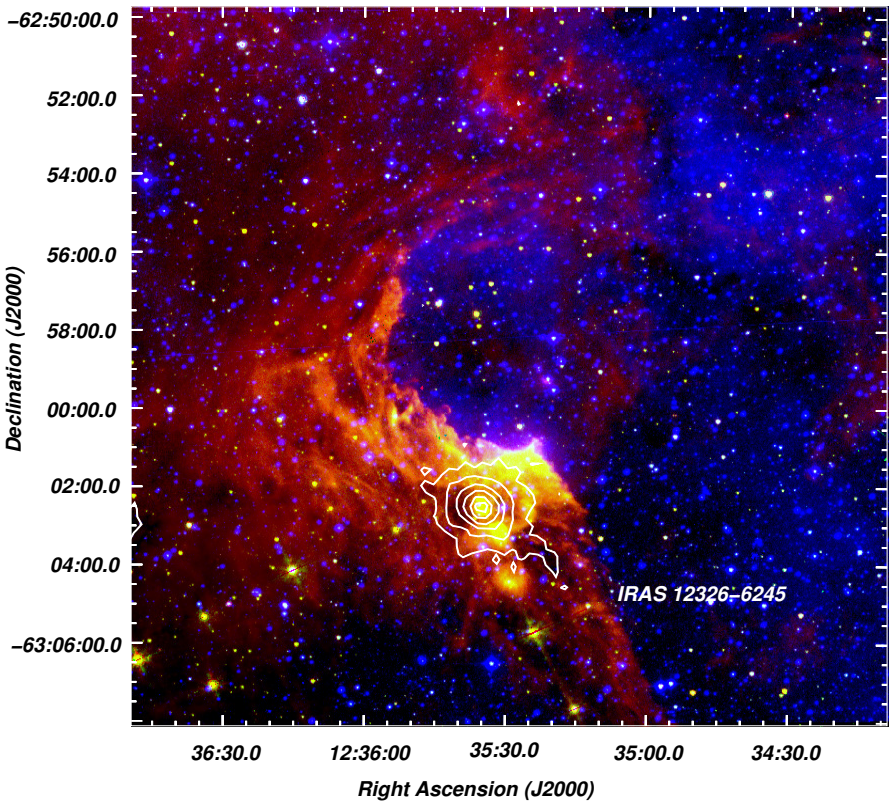


**Fig. 1.** Composite image of S169 and its environs showing the (IRAC-GLIMPSE) emission at 8.0 (red) and 5.8 $\mu$m (green) (IRAC-GLIMPSE). The superCOSMOS H$\alpha$ emission is in blue. White contours depict the continuum emission at 870 $\mu$m (ATLASGAL) arising from IRAS 12326-6245.

of S169 in 8.0 and 5.8 $\mu$m (IRAC-GLIMPSE) and the H$\alpha$ (superCOSMOS) emissions. The presence of emission in the 8-$\mu$m band, mostly dominated by the emission of polycyclic aromatic hydrocarbons molecules (PAHs) at 7.7 and 8.6 $\mu$m, indicates the existence of a photodissociation region (PDR) probably created by a near stellar source. Since PAHs molecules are destroyed inside the ionized gas of an HII region (Povich et al. 2007) but fluoresce when irradiated with weak ultra-violet radiation, they indicate the limits of the ionization front and delineate the boundaries of the bubble nebula, tracing the distribution of the parental molecular gas in which S169 is developing. This scenario is also supported by the presence of H$\alpha$ emission at the center of the bubble nebula. A distinctive feature in the emission of S169 is the presence of two bright borders at the southern region of the IR nebula, which are discernible in Fig. 1 in yellow tonalities. The spatial distribution of the IR emission gives a good hint of the distribution of the molecular gas and the location of the densest regions, very likely associated with the two bright borders described before. As can be seen from Fig.1, the IR emission at 8.0 $\mu$m toward the west is much weaker and composed by two faint arc-like filaments approximately at RA = $12^h35^m00^s$ and at RA = $12^h34^m10^s$.

The nebula S169 is placed near the IR source IRAS 12326-6245, which has characteristics of a young stellar object (YSO) according to the photometric criteria from Junkes et al. (1992). Several evidences suggest that IRAS 12326-6245 is a dense molecular core where massive star formation is taking place, namely: *a)* this source was observed in the CS(2-1) line at a velocity of $-39.4$ km s$^{-1}$ (Bronfman et al. 1996; Osterloh et al. 1997). It was also observed by Zinchenko et al. (2000) in several lines of HNCO at frequencies between 290 and 806 GHz. This indicates undoubtedly the existence of dense molecular gas associated with the source. *b)* emission from dense dust has been previously detected at 1.2mm as a compact source (Faúndez et al. 2004; Hill et al. 2005; Miettinen et al. 2006). The source is also a strong emitter at 870 $\mu$m (see Fig. 1 and Dedes et al. 2011). *c)* $CH_3OH$ maser emission, a common phenomenon in massive star forming regions, was reported by Caswell (2009) at a velocity of $-39.8$ km s$^{-1}$. OH and $H_2O$ maser emission was also detected at the source (Caswell 1998; MacLeod et al. 1998). *d)* a variety of complex organic molecules have been detected in the source (Araya et al. 2005; Dedes et al. 2011).This kind of molecules are mostly formed in the surface of dust grains and later evaporated to the gas phase. This is characteristic of "hot molecular cores" (HMC; Kurtz et al. 2000) which are better known to be associated with early stages of massive star formation. *e)* Molecular line maps indicate the presence of a very powerful bipolar outflow at the center of the source (Henning et al. 2000).

In this work, we present a complete multifrequency analysis of the ISM around S169 using high spatial resolution molecular observations, which are necessary to establish the excitation conditions in the molecular environs, to estimate their physical properties, and to investigate the kinematics of the region. The analysis of the molecular observations were complemented with an analysis of a multifrequency archival dataset, which together contribute to understand the impact of the stellar feedback and how the ionized gas interacts with its molecular environment. We have also investigated the status of the star formation in the region. In that context, the proximity between S169 and IRAS 12326-6245 will allow us to better understand the massive star formation process around IR dust bubbles. An analysis of dense molecular line tracers and submillimeter emission in IRAS 12326-6245 is also presented.

**Table 1.** Observational parameters for the observed transitions.

| molecular transition | Frequency (GHz) | Beam ($''$) | Velocity resolution (km s$^{-1}$) | rms noise (K) |
|---|---|---|---|---|
| CO(2-1) | 230.538000 | ~27 | 0.3 | ~0.3 |
| $^{13}$CO(2-1) | 220.398677 | ~28 | 0.3 | ~0.3 |
| C$^{18}$O(2-1) | 219.560357 | ~28 | 0.3 | ~0.25 |
| HCN(3-2) | 265.886180 | ~23 | 0.3 | ~0.15 |
| HCO$^+$(3-2) | 267.557526 | ~23 | 0.3 | ~0.15 |

The source IRAS 12326-6245 is believed to be placed at a distance of 4.4 kpc. Such distance was first estimated by Osterloh et al. (1997) and consistently adopted afterwards by several authors (e.g. Henning et al. 2000; Faúndez et al. 2004; Dedes et al. 2011). The distance to IRAS 12326-6245 will be also matter of some debate in this work.

## 2. Observations and databases

### 2.1. Molecular observations

The molecular observations presented in this paper were made during December 2016, with the Atacama Pathfinder EXperiment (APEX) telescope (Güsten et al. 2006) at Llano de Chajnantor (Chilean Andes). As front end for the observations, we used the APEX-1 receiver of the Swedish Heterodyne Facility Instrument (SHeFI; Vassilev et al. 2008). The back end for all observations was the eXtended bandwidth Fast Fourier Transform Spectrometer2 (XFFTS2) with a 2.5 GHz bandwidth divided into 32768 channels. The observed transitions and basic observational parameters are summarized in Table 1. Calibration was done by the chopper-wheel technique, and the output intensity scale given by the system is $T_{\rm A}$, which represents the antenna temperature corrected for atmospheric attenuation. The observed intensities were converted to the main-beam brightness temperature scale by $T_{\rm mb} = T_{\rm A}/\eta_{\rm mb}$, where $\eta_{\rm mb}$ is the main beam efficiency. For the APEX-1 receiver we adopted $\eta_{\rm mb} = 0.75$.

Observations were made using the on-the-fly (OTF) mode with a step size of 10$''$ (full sampling) in two orthogonal scan directions along RA and Dec.(J2000). For the lines CO(2-1), $^{13}$CO(2-1) and C$^{18}$O(2-1) the observed region was of ~14$'$×14$'$ in size centered on RA, Dec. (J2000)= ($12^{\rm h}35^{\rm m}44^{\rm s}$, $-63°00'08''$). For the lines HCN(3-2) and HCO$^+$(3-2) the observed region was ~4$'$×4$'$ in size centered on the position of the source IRAS 12326-6245 at RA, Dec. (J2000)= ($12^{\rm h}35^{\rm m}33^{\rm s}$, $-63°02'56''$).

The data reduction was carried out with the CLASS90 package of the IRAM GILDAS software[1].

### 2.2. Archival data

– Infrarred data: *a)* Images of ATLASGAL at 870 $\mu$m (345 GHz) (Schuller et al. 2009). This survey covers the inner Galactic plane, $l = 300°$ to $60°$, $|b| \leq 1.°5$, with a rms noise in the range 0.05 - 0.07 Jy beam$^{-1}$. The beam size at 870 $\mu$m is 19$''$.2. *b)* Images from the *Herschel*[2] Infrared GALactic (Hi-GAL) plane survey key program (Molinari et al. 2010). We used images from the photometric array camera and spectrometer (PACS) survey at 70 and 100 $\mu$m, with FWHM of 5$''$.5 and 11$''$, respectively, and from the spectral and photometric imaging receiver (SPIRE) at 350 $\mu$m with a FHWM of 25$''$. *c)* Images from *Spitzer* at 5.8 and 8.0 $\mu$m from the Galactic Legacy Infrared Mid-Plane Survey Extraordinaire (*Spitzer*-GLIMPSE, Benjamin et al. 2003a), retrieved from the Spitzer Science Center[3]. The images have a spatial resolution of ~ 2$''$.

– Radio continuum data: Mosaics obtained from the Sydney University Molonglo Sky Survey[4] (SUMSS; Bock et al. 1999). This wide-field radio imaging survey covers the southern sky at 843 MHz. The resolution is $43'' \times 43''cosec(\delta)$ and the rms noise level is ~ 1 mJy beam$^{-1}$.

– HI data: Data cubes from the Southern Galactic Plane Survey (SGPS; McClure-Griffiths et al. 2005). This survey includes the regions limited by Galactic longitude $253° \leq l \leq 358°$ (SGPS-1) and $5° \leq l \leq 20°$ (SGPS-2) and Galactic latitude $|b| \leq 1.°5$. Interferometric observations obtained with the Australia Telescope Compact Array (ATCA) are combined with single dish data from the 64-m Parkes radiotelescope. The final products have an angular resolution of 2 arcmin and an rms sensitivity of ~ 1 mJy beam$^{-1}$.

– Narrow-band H$\alpha$ data retrieved from SuperCOSMOS H$\alpha$ Survey[5] (SHS). The images have a spatial resolution of ~1$''$ (Parker et al. 2005).

– To investigate about ionizing stars candidates and YSO candidates in the region of the nebula, we made use of the IRAS Point Source Catalogue[6] (Beichman et al. 1988), the MSX Infrared Point Source Catalogue[7] (Egan et al. 2003), the WISE All-Sky Source Catalogue[8] (Wright et al. 2010), the GLIMPSE point source catalog[9] (Benjamin et al. 2003b), the Two Micron All Sky Survey (2MASS)[10] (Skrutskie et al. 2006), the American Association of Variable Star Observers (AAVSO) Photometric All-Sky SurveyA (APASS)[11] (Henden et al. 2010), the ASCC-2.5 V3: All-sky Compiled Catalogue of 2.5 million stars (Kharchenko & Roeser 2009), and the Astrometric catalogue GAIA Data Release 2 [12] (DR2; Gaia Collaboration et al. (2016, 2018)).

## 3. Molecular and dust emission

### 3.1. Emission of CO and its isotopologues

Fig. 2 portrays the total averaged spectra of CO(2-1), $^{13}$CO(2-1), and C$^{18}$O(2-1) in a region of ~14$'$×14$'$ in a position approximately at the center of the bubble nebula. The CO emission

[1] http://www.iram.fr/IRAMFR/GILDAS

[2] *Herschel* is an ESA space observatory with science instruments provided by European-led Principal Investigator consortia and with important participation from NASA (http://www.cosmos.esa.int/web/herschel/science-archive)

[3] http://scs.spitzer.caltech.edu

[4] http://www.astrop.physics.usyd.edu.au/mosaics

[5] http://www-wfau.roe.ac.uk/sss/halpha/hapixel.html

[6] https://irsa.ipac.caltech.edu/Missions/iras.html

[7] https://irsa.ipac.caltech.edu/Missions/msx.html

[8] https://irsa.ipac.caltech.edu/Missions/wise.html

[9] https://irsa.ipac.caltech.edu/Missions/spitzer.html

[10] https://irsa.ipac.caltech.edu/Missions/2mass.html

[11] https://www.aavso.org/apass

[12] https://www.cosmos.esa.int/web/gaia/home

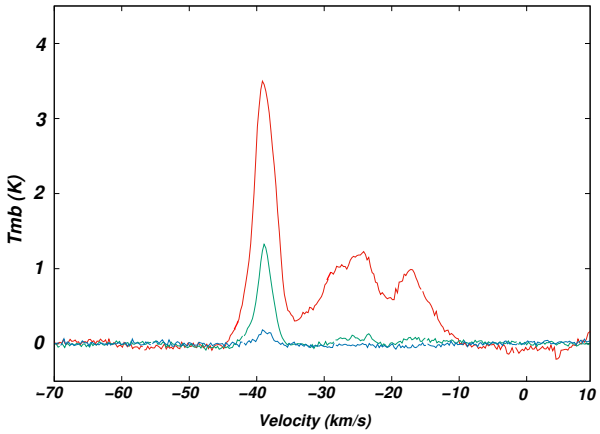


**Fig. 2.** Total averaged spectra of CO(2-1) (red), $^{13}$CO(2-1) (green), and C$^{18}$O(2-1) (blue) obtained within a region of ∼14′×14′ centered on RA, Dec. (J2000)= ($12^h35^m44^s$, −63°00′08″).

clearly depicts a strong narrow-velocity component peaking at ∼ −39 km s$^{-1}$ and two weaker broad-velocity components peaking at ∼ −25 km s$^{-1}$ and ∼ −17 km s$^{-1}$. For the sake of the analysis, these components will be hereafter referred to as Component A, Component B, and Component C, respectively.

The peak velocity of Component A is almost coincident with the peak velocity of reported non-masing and masing emission lines towards IRAS 12326-6245 (Bronfman et al. 1996; Zinchenko et al. 2000; Henning et al. 2000; Dedes et al. 2011; Araya et al. 2005; Caswell 1998, 2009; MacLeod et al. 1998), which suggests a physical association between S169 and the IRAS source. This component is also detected in $^{13}$CO and C$^{18}$O emissions, which indicates that it is composed of high-density molecular gas. Components B and C, on the other hand, are barely detected in the $^{13}$CO emission and not detected in the C$^{18}$O emission. As opposed to the case of the velocity of Component A, neither masing nor non-masing emission lines were reported for IRAS 12326-6245 at the velocity of Components B and C.

### 3.2. Component A

In Fig. 3 we show the spatial distribution of the CO(2-1), $^{13}$CO(2-1), and C$^{18}$O(2-1) lines in the velocity interval from ∼ −41 km s$^{-1}$ to −37 km s$^{-1}$. As expected according to the IR emission distribution (see Fig. 1), the bulk of the molecular emission appears concentrated toward the eastern and southern borders of the IR nebula, with no significant molecular emission detected toward the western and northeastern regions. The morphology and location of the molecular gas emission from Component A, H$\alpha$ emission (see Fig. 1) and radio continuum emission (see Sect. 4) suggest that the ionized gas is expanding against the molecular cloud in the eastern and southern borders. The molecular emission at the southern border of the bubble seems to be tracing the densest areas, which are probably sculpted by the action of the HII region. The morphology and location of Component A with respect to the near IR emission is similar to many other in Galactic IR bubbles found in the literature (e.g. Zavagno et al. 2006; Deharveng et al. 2008, 2009; Anderson et al. 2015; Liu et al. 2015; Cappa et al. 2016; Duronea et al. 2017; Devine et al. 2018).

From Fig. 3 it can also be seen that the CO emission of Component A is more extended than that of $^{13}$CO and C$^{18}$O. This indicates that $^{13}$CO and C$^{18}$O lines, optically thinner than that of CO (see below), are actually tracing the distribution of the densest molecular gas surrounding the bubble nebula. In order to perform a more detailed analysis of the dense molecular gas in Component A, we have roughly identified six molecular condensations in the $^{13}$CO(2-1) emission using the C$^{18}$O(2-1) emission map as a reference. They are labeled in Fig. 3 as MC1, MC2, MC3, MC4, MC5, and MC6. These condensations are the places where star formation is likely taking place (see Sect. 5). In Fig. 4 we show the channel maps of $^{13}$CO in the velocity range from −36 km s$^{-1}$ to −42 km s$^{-1}$ in intervals of 0.7 km s$^{-1}$. In order to compare the molecular emission distribution with the warm and cold dust emission, the $^{13}$CO emission was superimposed on the 8.0 and 5.8 $\mu$m (IRAC-GLIMPSE) and the 870 $\mu$m ATLASGAL maps. Fig. 4 shows that MC3, located at RA, Dec. (J2000)= ($12^h35^m35^s$, −63°02′25″), is the only molecular condensation that is present in the entire velocity range. The position and size of MC3 perfectly match with those of the bright spot seen at 870 $\mu$m. This condensation certainly represents the carbon monoxide counterpart of IRAS 12326-6245, which demonstrates without doubt the physical association between S169 and the IRAS source. In the velocity interval from −36.4 to −38.2 km s$^{-1}$ condensation MC1 becomes noticeable, reaching its peak temperature in the velocity interval from −38.9 to −39.6 km s$^{-1}$, close to a 8.0 $\mu$m source seen at RA, Dec. (J2000)= ($12^h35^m24^s$, −63°05′42″). It can be detected till a velocity of −40.4 km s$^{-1}$. For the case of condensation MC2, it can be first noticed in the velocity interval from −36.7 to −38.9 km s$^{-1}$, where its emission merges with MC1. Its peak emission is observed in the velocity range from −37.4 to −38.2 km s$^{-1}$ and is coincident with another 8.0 $\mu$m source seen at RA, Dec. (J2000)= ($12^h35^m29^s$, −63°04′25″). Condensation MC4 becomes detected in the velocity interval from −35.7 to −37.4 km s$^{-1}$, reaching to its maximum peak emission in the velocity interval from −32.2 to −38.9 km s$^{-1}$. It can be noticed till a velocity of −39.6 km s$^{-1}$ although its emission appears blended with MC2. Regarding condensations MC5 and MC6, they become detectable in the velocity range from −36.7 to −37.4 km s$^{-1}$. Their emission distribution is quite irregular and achieve their peak temperatures in the velocity range from −38.2 to −38.9 km s$^{-1}$. Condensation MC4 is detectable till a velocity of −39.6 km s$^{-1}$, while MC5 till a velocity of −40.4 km s$^{-1}$.

Figure 4 also shows a strong morphological correlation between the brightest parts of the PDR (described in Sect. 1) and the molecular condensations MC3, MC4 and MC5, specially at velocities between −38.2 to −38.9 km s$^{-1}$. Particularly, it is noticeable how the bright emission feature detected at 5.8 and 8.0 $\mu$m borders the area of MC3, which are likely exposed to stellar radiation.

To estimate the physical properties of the $^{13}$CO condensations, we have obtained six $^{13}$CO emission maps (not shown here) integrated in the velocity interval in which each condensation is detected. The deconvolved effective radius of the condensations derived from the $^{13}$CO line, $R_{\rm D}^{^{13}{\rm CO}}$, was calculated as

$$R_{\rm D}^{^{13}{\rm CO}} = \sqrt{R_{\rm eff}^2 - ({\rm HPBW}/2)^2}, \quad (1)$$

where $R_{\rm eff}$ is the effective radii of the condensation ($R_{\rm eff} = \sqrt{A_{\rm cond}/\pi}$), being $A_{\rm cond}$ the area of the condensation, and HPBW is the half-power beam width of the instrument. To estimate $R_{\rm D}^{^{13}{\rm CO}}$ and other parameters we adopted a distance of $2.03^{+0.77}_{-0.61}$ kpc (see Sect. 6.2). Then, we obtained the effective radii of 0.40, 0.27, 0.94, 0.49, 0.75, and 0.86 pc for MC1, MC2, MC3, MC4, MC5, and MC6, respectively.

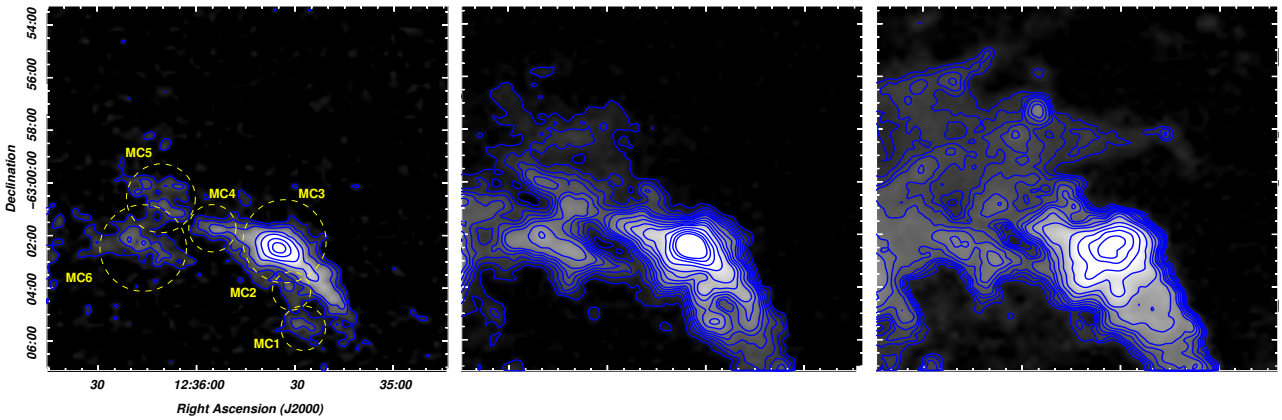


**Fig. 3.** Spatial distribution of the $C^{18}O$(2-1) emission (left panel), $^{13}CO$(2-1) emission (middle panel), and CO(2-1) emission (right panel) in the velocity interval from ~ –41 km s$^{-1}$ to –37 km s$^{-1}$ (Component A). In the left panel the contours are 0.35 (~ 3 rms), 0.7, 1.15, 2, 3, 5, and 7 K km s$^{-1}$. In the middle panel the contour levels are 0.5 (~ 6 rms), 1, 1.5, 2, 2.5, 3, 4, 5, 7, 9, 11, 13, and 15 K km s$^{-1}$. In the right panel the contour levels are 1.5 (~ 20 rms), 2, 2.5, 3, 4, 5, 6, 8, 10, 14, 18, 22, and 26 K km s$^{-1}$ ($T_{\rm mb}$). Identified molecular condensations are indicated in yellow over the $C^{18}O$(2-1) emission.

Assuming that all rotational levels are thermalized with the same excitation temperature (LTE) and that the emission is optically thick, we derived the excitation temperature of each molecular condensation, $T_{\rm exc}$, from the CO(2-1) line using

$$T_{\rm peak} = T^*_{12}\left[\left(e^{\frac{T^*_{12}}{T_{\rm exc}}}-1\right)^{-1}-\left(e^{\frac{T^*_{12}}{T_{\rm bg}}}-1\right)^{-1}\right], \quad (2)$$

where $T^*_{12} = h\nu_{12}/k$, being $\nu_{12}$ the frequency of the $^{12}CO$(2-1) line, and $T_{\rm bg}$ = 2.7 K. To obtain the peak main beam temperature of the CO(2-1), $^{13}CO$(2-1), and $C^{18}O$(2-1) lines ($T_{\rm peak}$) we used Gaussian fits over the spectra profiles obtained integrating in the direction of the peak emission of the $^{13}CO$ condensations (in all the cases coincident with those of the $C^{18}O$ emission) over an area equivalent to the area of the beam. It is worth to point out that a single Gaussian component was considered for MC3, which shows self-absorption in the spectrum of CO(2-1) at the velocity of the peak emission of $^{13}CO$(2-1) and $C^{18}O$(2-1) (not shown here) due to the presence of a powerful outflow (Henning et al. 2000; Dedes et al. 2011). Excitation temperatures derived with Eq. 2 are then 21.3 K, 33.8 K, 47.8 K, 21.2 K, and 16.0 K, and 16.8 K for MC1, MC2, MC3, MC4, MC5, and MC6, respectively.

The optical depths ($\tau$) of the $^{13}CO$(2-1) and $C^{18}O$(2-1) lines, denoted in the next equations as $\tau^{13}$ and $\tau^{18}$, respectively, were obtained assuming that the excitation temperature is the same for CO(2-1), $^{13}CO$(2-1), and $C^{18}O$(2-1), and using the expressions

$$\tau^{13} = -\ln\left[1-\frac{T_{\rm peak}{}^{13}{\rm CO}}{T^*_{13}}\left[\left(e^{\frac{T^*_{13}}{T_{\rm exc}}}-1\right)^{-1}-\left(e^{\frac{T^*_{13}}{T_{\rm bg}}}-1\right)^{-1}\right]^{-1}\right], \text{and} \quad (3)$$

$$\tau^{18} = -\ln\left[1-\frac{T_{\rm peak}{\rm C}^{18}{\rm O}}{T^*_{18}}\left[\left(e^{\frac{T^*_{18}}{T_{\rm exc}}}-1\right)^{-1}-\left(e^{\frac{T^*_{18}}{T_{\rm bg}}}-1\right)^{-1}\right]^{-1}\right], \quad (4)$$

where $T^*_{13} = h\nu_{13}/k$, $T^*_{18} = h\nu_{18}/k$, being $\nu_{13}$ and $\nu_{18}$ the frequencies of the $^{13}CO$(2-1) and $C^{18}O$(2-1) lines, respectively. We can also estimate the optical depth of the CO(2-1) line from the $^{13}CO$(2-1) line using

$$\tau^{12} = \left[\frac{\nu^{13}}{\nu^{12}}\right]^2 \times \left[\frac{\Delta{\rm v}^{13}}{\Delta{\rm v}^{12}}\right] \times \left[\frac{\rm CO}{^{13}{\rm CO}}\right] \tau^{13}, \quad (5)$$

where CO/$^{13}$CO is the isotope ratio (assumed to be ~ 62; Langer & Penzias 1993); $\Delta{\rm v}^{13}$ and $\Delta{\rm v}^{12}$ are defined as the *full width half maximum* (FWHM) of the spectra of the $^{13}CO$ and CO lines, respectively, which are derived by using a single Gaussian fitting (FWHM = $2\times\sqrt{2\,ln2}\times\sigma_{\rm gauss}$).

In LTE, the $^{13}CO$ and $C^{18}O$ column densities can be estimated from the $^{13}CO$(2-1) and $C^{18}O$(2-1) line using

$$N(^{13}{\rm CO}) = 3.23\times10^{14}\left[\frac{e^{\frac{T^*_{13}}{T_{\rm exc}}}}{1-e^{-\frac{T^*_{13}}{T_{\rm exc}}}}\right]T_{\rm exc}\int\tau^{13}\,dv \quad ({\rm cm}^{-2}), \text{and} \quad (6)$$

$$N({\rm C}^{18}{\rm O}) = 3.21\times10^{14}\left[\frac{e^{\frac{T^*_{18}}{T_{\rm exc}}}}{1-e^{-\frac{T^*_{18}}{T_{\rm exc}}}}\right]T_{\rm exc}\int\tau^{18}\,dv \quad ({\rm cm}^{-2}) \quad (7)$$

The integral in Eqs. 6 and 7 can be approximated by

$$T_{\rm exc}\int\tau\,dv \approx \frac{\tau}{1-e^{(-\tau)}}\int T_{\rm mb}\;{\rm dv}. \quad (8)$$

This approximation helps to eliminate to some extent optical depth effects and is good within 15% for $\tau < 2$ (Rohlfs & Wilson 2004). Bearing in mind the values of $\tau^{13}$ obtained, the approximation is appropriate for our region. Estimations of the $H_2$ column density, $N(H_2)$, were obtained from both the $^{13}CO$ and $C^{18}O$ column densities, and adopting abundances $X[^{13}{\rm CO}] = 7.1\times10^5$ and $X[{\rm C}^{18}{\rm O}] = 5.9\times10^6$ (Frerking et al. 1982).

The total hydrogen mass of each clump was calculated using

$${\rm M(H_2)} = (m_{\rm sun})^{-1}\,\mu\,m_{\rm H}\,\Omega\,N({\rm H_2})\,d^2 \qquad ({\rm M_\odot}) \quad (9)$$

where $m_{\rm sun}$ is the solar mass (~$2\times10^{33}$ g), $\mu$ is the mean molecular weight, which is assumed to be equal to 2.76 after allowing for a relative helium abundance of 25% by mass (Yamaguchi et al. 1999), $m_{\rm H}$ is the hydrogen atom mass (~$1.67\times10^{-24}$ g), $\Omega$ is the solid angle of the $^{13}CO$ emission expressed in sr, $d$ is the adopted distance expressed in cm, and $N(H_2)$ is the $H_2$ column density obtained from $N(^{13}CO)$. Uncertainties in molecular masses are about 60%, and originate mainly from a distance uncertainty of about 30 % (see Sect. 6.2). The derived physical parameters are presented in Table 2.

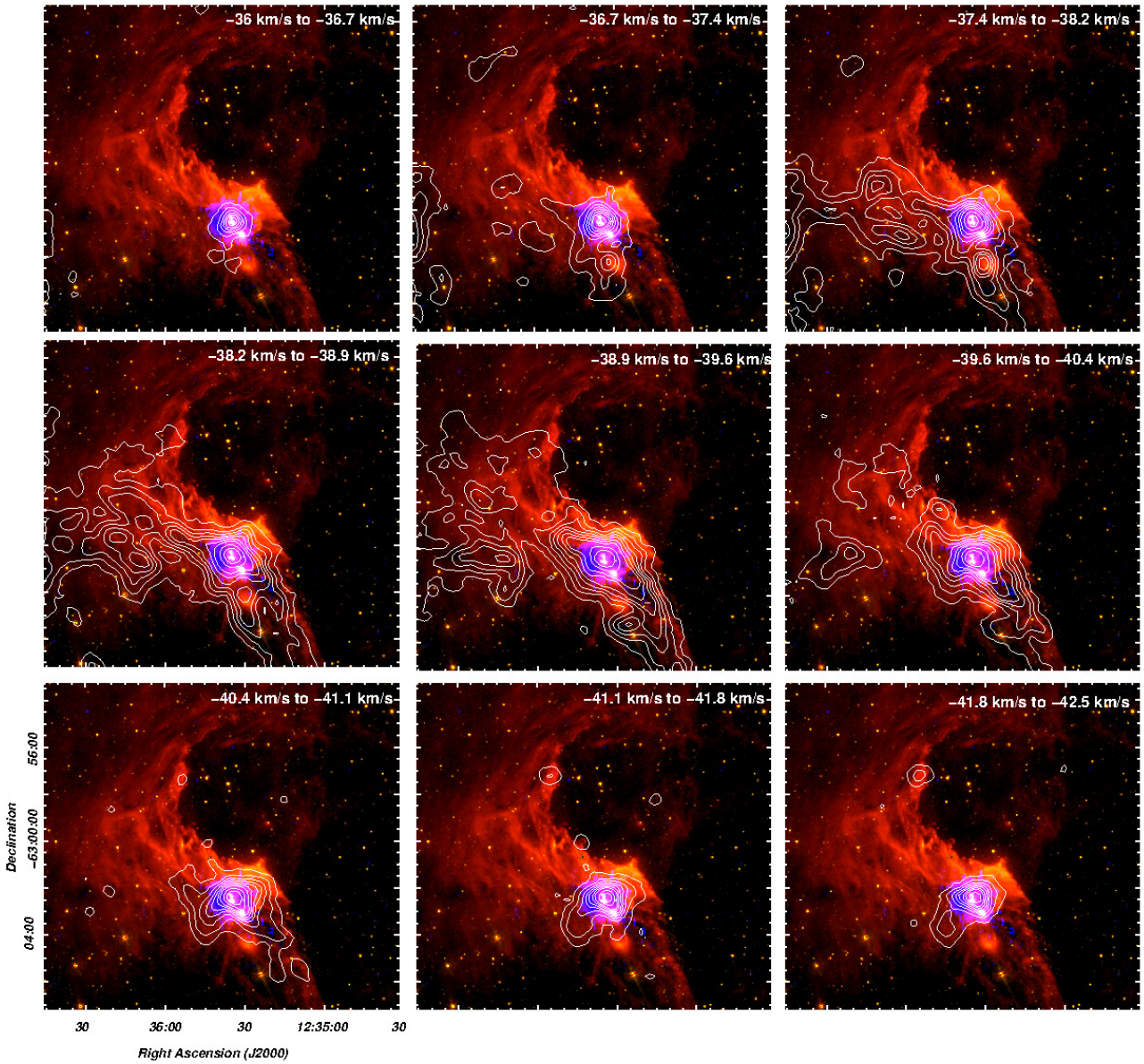


**Fig. 4.** Channel maps of the $^{13}$CO(2-1) line emission in velocity intervals of 0.7 km s$^{-1}$ (white contours) superimposed on the 8.0 $\mu$m and 5.8 $\mu$m (IRAC-GLIMPSE) emissions (red and green color scales) and 870 $\mu$m ATLASGAL emission (blue color scale) inside the 3 rms limit. Contours levels are 0.9 ($\sim$ 5.5 rms), 2.6, 4.4, 6.2, 7.9, 10, 12, 16, and 20 K km s$^{-1}$. The velocity interval is indicated in the top right corner of each panel.

**Table 2.** Observed parameters obtained from the emission lines and physical properties derived for the molecular condensations MC1 to MC6

| | $T_{peak}$ (K) CO $^{13}$CO C$^{18}$O | $\int T_{mb}\,dv$ (K km s$^{-1}$) $^{13}$CO C$^{18}$O | $\Delta$v (km s$^{-1}$) CO $^{13}$CO | $\tau$ CO $^{13}$CO C$^{18}$O | $N(^{13}CO)$ (cm$^{-2}$) | $N(C^{18}O)$ (cm$^{-2}$) | $N(H_2)$ (cm$^{-2}$) | $M(H_2)$ ($M_\odot$) |
|---|---|---|---|---|---|---|---|---|
| MC1 | 16.1 6.8 0.8 | 15.9 0.7 | 2.75 1.49 | 16.51 0.54 0.05 | $2.8\times10^{16}$ | $1.0\times10^{15}$ | $(2.0/0.6)\times10^{22}$ | 300 |
| MC2 | 28.4 10.0 1.3 | 7.8 1.0 | 2.85 1.91 | 16.32 0.43 0.04 | $1.6\times10^{16}$ | $1.6\times10^{15}$ | $(1.2/0.9)\times10^{22}$ | 90 |
| MC3 | 42.2 23.3 7.1 | 32.8 8.1 | 7.51 5.85 | 36.2 0.83 0.19 | $9.8\times10^{16}$ | $1.8\times10^{16}$ | $(1.0/0.7)\times10^{23}$ | 5500 |
| MC4 | 15.9 7.4 2.1 | 9.9 1.2 | 2.83 2.16 | 26.38 0.61 0.13 | $1.8\times10^{16}$ | $1.1\times10^{15}$ | $(1.3/0.7)\times10^{22}$ | 280 |
| MC5 | 10.9 6.9 1.6 | 6.1 0.8 | 3.18 1.59 | 27.76 0.98 0.15 | $1.2\times10^{16}$ | $1.1\times10^{15}$ | $(8.5/6.5)\times10^{21}$ | 420 |
| MC6 | 11.7 8.4 1.3 | 7.1 1.1 | 2.55 1.65 | 44.36 1.21 0.11 | $1.6\times10^{16}$ | $1.5\times10^{15}$ | $(1.2/0.9)\times10^{22}$ | 720 |

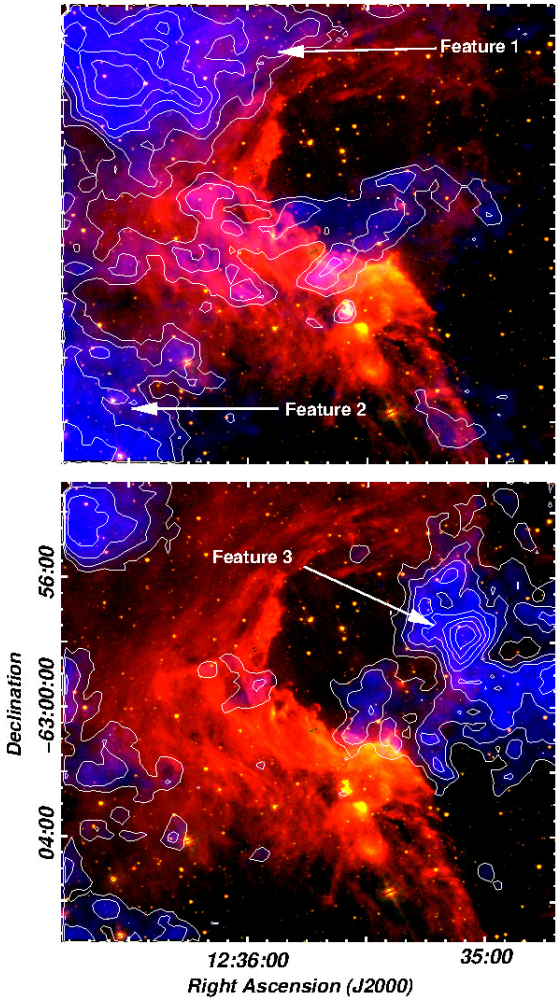


**Fig. 5.** *Upper panel:* Spatial distribution of the CO emission (in blue color scale) in the velocity interval from −28.9 km s$^{-1}$ to −18.9 km s$^{-1}$ (Component B) superimposed on the IRAC 8 $\mu$m and 5.8 $\mu$m emissions (red and green color scales). The contour levels start from 0.95 K km s$^{-1}$ (∼ 9 rms) in steps of 0.5 K km s$^{-1}$. *Lower panel:* Spatial distribution of the CO emission in the velocity interval from −18.2 km s$^{-1}$ to −12.7 km s$^{-1}$ (Component C). The contour levels start from 0.85 K km s$^{-1}$ (∼ 7 rms) in steps of 0.4 K km s$^{-1}$.

In order to perform a more detailed study of the molecular gas and dust in IRAS 12326-6245, a more sophisticated analysis for MC3, using the high density tracer lines HCN(3-2) and HCO$^+$(3-2) and the continuum emission at 870 $\mu$m, is presented in Sect. 5.3.

### 3.3. Components B and C

As mentioned in Sect. 3.1, two weaker broad-velocity molecular components peaking approximately at −25 km s$^{-1}$ (Component B) and −17 km s$^{-1}$ (Component C) were also detected in S169. These components are hardly detected in the $^{13}$CO emission and not detected at all in the C$^{18}$O emission, which certainly indicates that they are mostly composed by low-density gas. In order to analyze their spatial distribution we have constructed two CO emission maps integrated in the velocity intervals from −28.9 to −18.9 km s$^{-1}$ (Component B) and from −18.2 to −12.7 km s$^{-1}$ (Component C). They are shown in Fig. 5 superimposed on the 8.0 and 5.8 $\mu$m emissions. For the case of Component B, three molecular features are seen projected towards different regions of the nebula. The brightest feature (hereafter Feature 1) is seen approximately centered at RA, Dec. (J2000)= ($12^h36^m34^s$, $-62°55'13''$) perfectly delineating the northeastern and northern borders of the IR nebula. As can be seen from the figure, the brightest regions of the molecular gas appear projected onto the faintest regions of the IR emission, which suggests that a PDR was formed over the surface of Feature 1 (viewed from the side). Another feature is seen centered approximately at RA, Dec. (J2000)= ($12^h36^m40^s$, $-63°06'00''$) (Feature 2). This feature appears bordering the southeastern edge of the nebula, also projected onto the faintest regions of the IR nebula. The third feature is seen projected along the center of the nebula approximately at Dec=$-62°58'00''$ and is still noticeable at more negative velocities. Since this feature shows no morphological correspondence with any region of the IR nebula, a physical link with S169 cannot be suggested. Probably, it is an unconnected molecular structure located behind the nebula since no absorption features can be noticed along the brightest regions of the IR emission. Regarding Component C, only one molecular structure (Feature 3) stands out peaking approximately at RA, Dec. (J2000)= ($12^h35^m05^s$, $-62°58'00''$). This feature shows a good morphological correspondence with the faint IR arc-like filament seen at the western section of the nebula at RA = $12^h35^m00^s$. The feature seems to be part of a larger structure that extends towards the western regions, near the second weaker IR filament at RA = $12^h33^m30^s$ depicted in Fig.1. Another structure is noticed at the northeastern region of the nebula although it represents the remains of Feature 1 at slightly more positive velocities.

**Table 3.** Physical properties estimated for the CO Feature 1, Feature 2, and Feature 3

| Feature | $\Omega$ ($10^{-6}$ sr) | $\int T_{\rm mb}$(CO) $dv$ (K km s$^{-1}$) | $N$(H$_2$) ($10^{20}$cm$^{-2}$) | $M$(H$_2$) ($M_\odot$) |
|---|---|---|---|---|
| 1 | 2.4 | 14.9 | 2.4 | 52 |
| 2 | 1.3 | 12.3 | 2.0 | 24 |
| 3 | 2.5 | 7.9 | 1.3 | 29 |

Since no discernible emission of the $^{13}$CO(2-1) line is detected for Features 1, 2, and 3, to estimate their column density and mass we use the relation between the H$_2$ integrated column density and the CO integrated emission

$$N(\mathrm{H_2}) = X \times \int T_{\rm mb}(\mathrm{CO})\, dv, \qquad (10)$$

where $X$ is an empirical factor that has been shown to be roughly constant for the $^{12}$CO(1-0) line in Galactic molecular clouds and lies in the range (1 - 3) × $10^{20}$ cm$^{-2}$ (K km s$^{-1}$)$^{-1}$, as estimated by the virial theorem and $\gamma$-ray emission (Bloemen et al. 1986; Solomon et al. 1987; Digel et al. 1996; Strong & Mattox 1996). In this paper we adopt $X = 1.6 \times 10^{20}$ cm$^{-2}$ (K km s$^{-1}$)$^{-1}$ (Hunter et al. 1997). The integrated emission $\int T_{\rm mb}$(CO) $dv$ was calculated adopting an area determined by the first contour level indicated in Fig. 5. The mass of the features were then estimated using Eq. 9. The obtained parameters are shown in Table 3. It is worth to point out that the area and mass obtained for Features 1 and 2 are likely lower limits since these features seem to be part of a larger structure (extending beyond the area covered in our APEX observations) which probably corresponds to the parental molecular cloud in which the IR bubble was formed.

### 3.4. Submillimeter dust emission

In the upper panel of Fig. 6 we present a three-color composite image of S169 as seen by *Herschel* images. The 70 and 160 $\mu$m emissions (red and green color-scales, respectively) underline the emission of the warmer dust close to the ionized gas. As can be seen from the figure, the emission at 70 $\mu$m has a good morphological correspondence with the IRAC 8 $\mu$m emission (black contours), although the latter exhibits a sharper edge towards the center of the nebula (see also Fig.1), likely due to the destruction of the PAH molecules by the ionization front. The 70 $\mu$m emission, in contrast, is more diffuse (partly because of the lower angular resolution) and extends towards the center of the nebula, which indicates that it is also tracing the warm dust that still remains mixed with the ionized gas. The same feature can be observed in the IRAC-GLIMPSE 24 $\mu$m emission (not shown here). The 350 $\mu$m emission (blue color-scale) seems to be underlining the emission from the dust in the outer parts of the nebula. Very likely, the emission distribution at this wavelength is mostly tracing the distribution of the cold dust immersed in the parental molecular cloud placed at the eastern border of the nebula, which is partially disclosed by Features 1 and 2 (see Fig. 5).

To study the distribution of the dust temperature in the nebula, we constructed a temperature map from the ratio of the observed fluxes in two *Herschel* bands. Since a high level of radiative feedback from powering massive stars is usually observed in HII regions/IR bubbles, it is reasonable to assume that the molecular gas and dust are not too cold. Then, we used the ratio of the 70 $\mu$m versus 160 $\mu$m maps, which are better suited to measure color temperatures up to $\sim$ 80 K. Furthermore, the angular resolution of the temperature map obtained using these bands is the highest resolution achievable from the *Herschel* maps. The 70 $\mu$m map was smoothed down to the angular resolution of the 160 $\mu$m data. Then, the pixel-to-pixel temperature map was constructed as the inverse function of the ratio 70 to 160 $\mu$m maps i.e., $T_c = f_{(T)}^{-1}$. Assuming a dust emissivity following a power law $\kappa_\nu \propto \nu^\beta$, being $\beta$ the spectral index of the thermal dust emission (assumed to be $\beta = 2$), in the optically thin thermal dust emission regime $f_{(T)}$ has the parametric form:

$$f_{(T)} = \frac{S_{70}}{S_{160}} = \frac{B(70,T)}{B(160,T)} \left(\frac{70}{160}\right)^{\beta} \quad (11)$$

where $B(70,T)$ and $B(160,T)$ are the blackbody Planck function for a temperature $T$ at wavelengths 70 and 160 $\mu$m, respectively. From the obtained map (middle panel of Fig. 6) dust temperatures between $\sim$ 20 and 30 K are discerned. These temperatures are commonly observed in the closest regions of IR bubble nebulae (e.g. Anderson et al. 2012; Duronea et al. 2015; Figueira et al. 2017). Warmer dust is seen in the region of the denser molecular condensations (MC1, MC2, MC3, and MC4) and the border of the PDR, particularly on two spots at RA, Dec. (J2000)= ($12^h35^m24^s$, $-63°00'56''$) and RA, Dec. (J2000)= ($12^h35^m35^s$, $-63°02'29''$) where the temperature achieves $\sim$ 30 K. The first spot is coincident with a bright rim placed over the southern region of the PDR and a peak in the radio continuum emission (see Fig.7 in Sect. 4) which suggests external heating of the dust. The second spot is coincident with the molecular condensation MC3 (IRAS12326-6245) which very likely indicates that the dust is also internally heated. Not surprisingly, lower temperatures (12 - 18 K) are seen in the region of Feature 3 and behind the PDR, coincident with the position of Features 1 and 2.

Having the temperature map, we converted the surface brightness map at 160 $\mu$m into a pixel-to-pixel beam-averaged column density map using

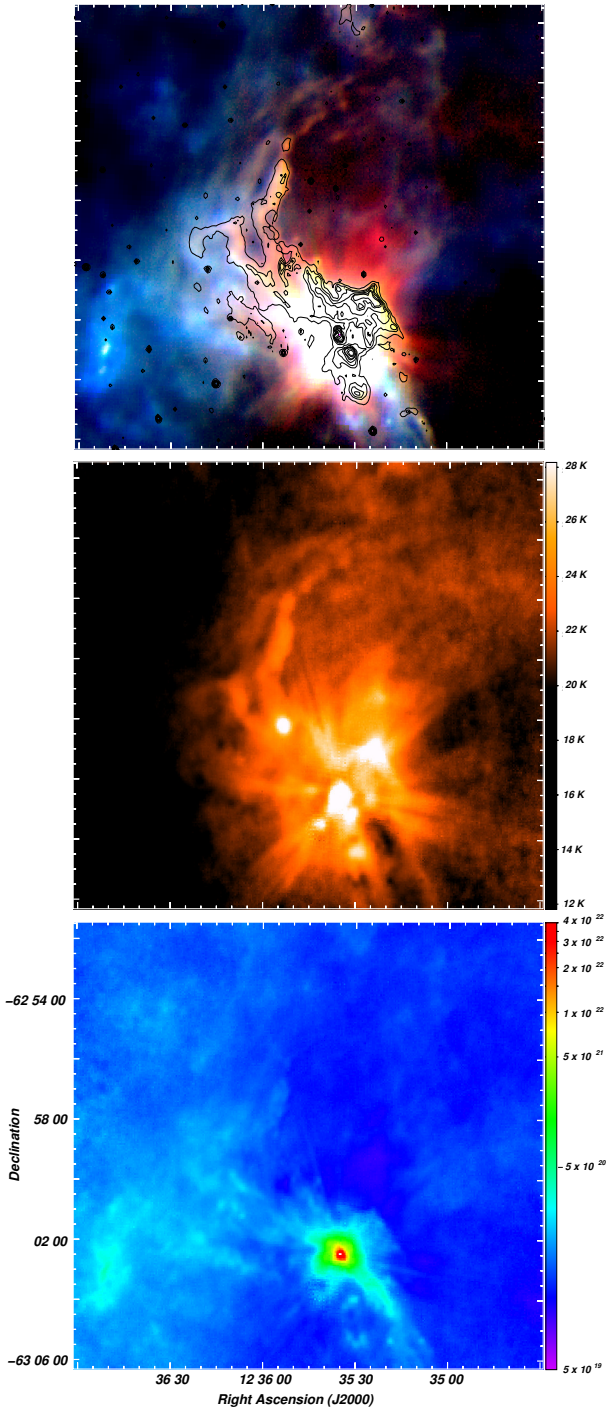


**Fig. 6.** *Upper panel:* Three-color composite image of S169: *Herschel* PACS 70 and 160 $\mu$m emission are in red and green, respectively. *Herschel* SPIRE 350 $\mu$m emission is in blue. Black contours underline de IRAC-GLIMPSE 8 $\mu$m emission at 35, 55, 75, 105, 150, 170, 300, and 500 MJy sr$^{-1}$. *Middle panel:* Dust temperature map derived from the 70 and 160 $\mu$m emission. The color-temperature scale is on the right. *Lower panel:* Column density map obtained from the 160 $\mu$m emission.

$$N(\mathrm{H_2}) = R \, \frac{S_{160}}{\Omega_{\mathrm{beam}} \, \kappa_{160} \, \mu \, m_{\mathrm{H}} \, B(160, T_{\mathrm{dust}})} \quad (12)$$

(Hildebrand 1983), where $\Omega_{\mathrm{beam}}$ is the beam solid angle ($\pi \, \theta^2_{\mathrm{HPBW}}$ / 4 ln 2), $R$ is the gas-to-dust ratio (assumed to be 100), and $\kappa_{160}$ is the dust opacity per unit mass at 160 $\mu$m assumed

to be 40.5 cm$^2$ g$^{-1}$ (Ossenkopf & Henning 1994). The resulting map (presented in the lower panel of Fig. 6) gives an overall view of the density distribution in the whole region of the nebula. Clearly, denser regions are observed behind the PDR in the region of Component A, especially towards IRAS12326-6245, where the column density achieves peak values up to $\sim 4{\times}10^{22}$ cm$^{-2}$. For this source, we have used the emission at 870 $\mu$m (a much more suitable emission to analyze dense gas) to derive its column density more properly (see Sect. 5.3).

## 4. Ionized gas

In Fig. 7 we show the radio continuum emission map at 843 MHz overlaid on the 8.0 and 5.8 $\mu$m emissions. Three bright structures stand out in the direction of the nebula. The brighest one ($S_{843}$ = 985 mJy), which does not have a discernible counterpart in the H$\alpha$ emission, is observed towards the norther border of the nebula at RA, Dec. (J2000)=($12^h35^m39^s$, $-62°54'26''$). Using a radio continuum image from the SGPS (not shown here), we found that this compact source has an integrated flux density of $S_{1384}$ = 0.63 mJy. Since the spectral index turns out to be $\alpha = -0.9$, we conclude that this source is extragalactic and will not be taken into further consideration.

An arc-shaped structure can be discerned towards the center of the nebula, which can be described by two main components: (i) a southern bright component with its outer edge closely delineating the PDR depicted by the 8.0 $\mu$m emission, and (ii) a weaker tail about 5′-long extending from the northern end of the previous component towards the northwest. A number of artifacts in the radio continuum emission are obviously produced by sidelobes and grating rings from the bright extragalactic source, like a void at RA, Dec. (J2000)≈($12^h35^m45^s$, $-62°56'33''$) and two radial strips connecting the compact source and the weak tail. Hence, we believe that the morphology of the arc-shaped structure is probably distorted in the region closer to the extragalactic source. However, the morphology of the unaffected part (southernmost component) suggests that the ionized gas traced by the radio continuum emission is likely expanding against Component A and Features 1 and 2, supporting the same conclusion previously derived in Sect. 1 based on the H$\alpha$ emission.

Using the integrated radio continuum flux (assumed to be optically thin) obtained for the whole arc-like structure ($S_{843}$ = 308 mJy), we obtained its electron density and ionized mass using

$$n_e = 3.113{\times}10^2\, S_{843}^{0.5}\, T_e^{0.25}\, d^{-0.5}\, b(\nu, T_e)^{-0.5}\, \theta_R^{-1.5}\ \mathrm{cm}^{-3}, \text{and} \quad (13)$$

$$M_{ion} = 0.7934\, S_{843}^{0.5}\, T_e^{0.25}\, d^{2.5}\, b(\nu, T_e)^{-0.5}\, \theta_R^{1.5}\ (1+Y)^{-1}\ \mathrm{M}_\odot, \quad (14)$$

(Panagia & Walmsley 1978), where $T_e$ is the electron temperature (assumed to be $1 \times 10^4$ K) in units of $10^4$ K, $\theta_R$ is the angular radius of the source in arc minutes (assumed to be 4′), $b(\nu, T_e)$ = 1 + 0.3195×log($T_e$/$10^4$ K) - 0.213×log($\nu$/1 GHz), $d$ is in kpc, and $Y$ is the abundance ratio by number of $He^+$ to $H^+$. Then, we obtained $n_e$ = 15 cm$^{-3}$ and $M_{ion}$ = 17 M$_\odot$.

The number of ionizing Lyman continuum photons needed to sustain the current level of ionization in the arc-like structure can be calculated using

$$N_{Lyc} = 0.76 \times\ 10^{47}\, T_e^{-0.45}\, S_{843}\, \nu^{0.1} d^2\ \mathrm{s}^{-1} \quad (15)$$

(Chaisson 1976), where $T_e$ is in units of $10^4$ K, $S_{843}$ is in Jy, $\nu$ is in GHz, and $d$ is in kpc. Then, considering distance uncertainties we obtained for this source a range $N_{Lyc}$ = 0.5 - 2.0 × $10^{47}$ s$^{-1}$. We keep in mind that this values are likely lower limits since about 25 - 50 % of the UV photons are absorbed by interstellar dust in the HII region (Inoue 2001). Further, Watson et al. (2008), on the basis of studies of several bubbles, concluded that $N_{Lyc}$ estimated with this method is lower than expected by about a factor of 2. Then for the arc-like structure we estimate a range $N_{Lyc} \approx$ (1 - 4) × $10^{47}$ s$^{-1}$. Adopting ionizing photon rates extracted from Martins et al. (2005), we estimate the spectral type of the ionizing star of S169 to be at most O9.5V. Alternatively, a handful of later B-type stars could also be responsible for powering the HII region. The third structure detected in the 843 MHz emission is a small bright spot discernible in the southern region of the nebula at RA, Dec. (J2000)= ($12^h35^m35^s$, $-63°02'29''$) which is certainly the radio continuum counterpart of IRAS12326-6245. Using the flux density obtained for this source ($S_{843}$=12 mJy) we obtained $n_e$ = 70 cm$^{-3}$, $M_{ion}$ = 0.3 M$_\odot$, and $N_{Lyc}$= (0.4 - 1.4) × $10^{46}$ s$^{-1}$. The latter value may represent a lower limit since the dust mixed in the high-density gas in the region (see Sect. 5.3) could be absorbing the bulk of the ionizing photons.

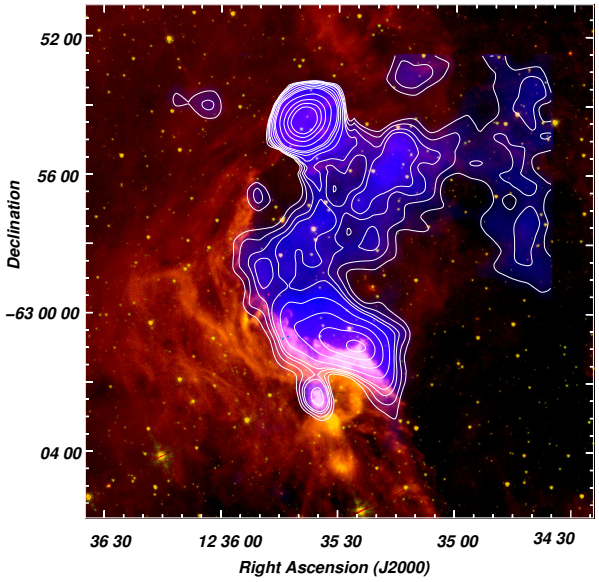


**Fig. 7.** Radio continuum emission distribution at 843 MHz (blue color and white contours), superimposed on the 8 and 5.8 $\mu$m emission (red and green color). Contours levels are 3.1 (~ 3 rms), 4.5, 6.3, 7.6, 12, 20, 30, 40, 100, 200, 300, and 400 mJy beam$^{-1}$.

Broadly, the distribution of the ionized gas suggests an electron density gradient, with the densest material near the border of the IR nebula. This configuration indicates that the nebula is bounded by density to the west, and bounded by ionization to the east, north, and south. Further, the structure detected to the west of the nebula along RA ~ $12^h34^m44^s$, which appears connected with the arc-shaped structure within the 3 rms emission limit, might be indicative of a 'champagne-flow' scenario (Tenorio-Tagle 1979).

## 5. Stellar and protostellar content in the nebula

### 5.1. Ionizing star candidates

Aiming to identify possible ionizing stars in the nebula, we first inspected IR catalogues in a region ~ 7′ in radius centered on RA, Dec. (J2000)≈($12^h35^m28^s$, $-62°58'04''$). Making use of GLIMPSE data we identified Class III candidates, which are usually referred to as main-sequence (MS) young stars, using color-color diagrams (Allen et al. 2004). Then, we cross-correlated these sources with sources selected from the 2MASS

catalogue with photometric uncertainty $K_s < 0.05$ mag (Ducati et al. 2001) and we obtained ~ 600 Class III sources with reliable $JHK$ photometry. Since none of these sources were found to have spectral classification we used the parameter $Q_{NIR} = (J-H)-1.7(H-K_s)$ following Borissova et al. (2011) to separate sources between early (O-B) MS stars (-0.1< $Q_{NIR}$ <0.15) and stars revealing IR excess ($Q_{NIR}$ < –0.1), which are likely pre-MS stars and/or YSOs. Then, we obtained 60 MS candidates.

Next, we inspected visual catalogues in the same region. A search in the APASS and ASCC-2.5 V3 catalogues yielded 228 and 10 sources with V and B magnitudes, respectively. We also carried out a search in the astrometric catalogue GAIA DR2 with more than 6000 sources with parallax data in the region of S169. We cross-correlated those 6000 sources with the 238 sources found with both, the APASS and ASCC-2.5 V3 catalogues, which yielded 90 sources in common. Among these 90 sources, only 19 had distance of 1.7 < d < 2.4 kpc (estimated from the parallax catalogued for each source). Then, we were able to confirm that 71 sources of the 90 found in common between the visual sources (238) and the astrometric sources (6000) did not have a distance of ~ 2 kpc. Thus, to estimate the distance of the remaining 167 (238 - 71) visual sources we used their color excess E($B-V$) which allowed us to estimate their spectral type via their positions in the color-magnitude diagram ($B-V$ vs $V$). We used the optical ($BV$) calibration given by Schmidt-Kaler (Th. 1982) to adjust the theoretical MS by a distance of 2 kpc (Distance Module = 11.5 mag) and color excess E ($B-V$) = 0.8 magnitudes.

Thereafter, we cross-correlated the 60 possible early MS stars obtained from the IR data with the 167 remaining sources with V and B magnitudes and we found 47 sources in common. In order to improve their spectral types, we inspected their loci in the two-color diagram ($J-H$) vs. ($H-K$) adopting the MS calibration given by Schmidt-Kaler (Th. 1982), Cousins (1978), and Koornneef (1983), the absorption ratios ($r_x = A_x/A_v$) given by Rieke & Lebofsky (1985), van der Hulst curve 15, and the color transformations from 2MASS to Koorneef data of Carpenter et al. (2001). As a final step, we kept only those stars that are projected onto the cavity of the bubble (~ 3′ in radius centered on RA, Dec. (J2000)≈($12^h35^m28^s$, $-62°58'04''$)) which yielded only 10 sources with spectral types O9 (2 sources), B1 (1 source) and B2 or later (7 sources), all of them probable MS. Their position in the cavity are shown in Fig. 8. It is worth to point out that only 5 of these sources belong to the group of 19 sources with distances between 1.7 kpc and 2.4 kpc obtained from GAIA.

### 5.2. Identification of candidate YSOs

Making use of the MSX, WISE and *Spitzer* point source catalogues, we look for the primary tracers of stellar formation activity onto the molecular clouds related to S169. To this aim, MSX sources were selected satisfying a flux quality Q >1 in the four bands. WISE sources with photometric flux uncertainties > 0.2 mag and signal-to-noise ratio < 7 in the W1, W2, W3, and W4 bands, were rejected. Finally, we kept *Spitzer* sources with photometric uncertainties < 0.2 mag in the four IRAC bands. Then, within a 14-arcmin box centered at RA, Dec. (J2000)= ($12^h35^m44^s$, $-63°00'08''$), we found a total of 2 MSX, 400 WISE, and 810 *Spitzer* sources fulfilling the selection criteria mentioned above. To identify candidate YSOs we adopted the classification scheme described in Lumsden et al. (2002), Koenig et al. (2012), and Gutermuth et al. (2009) for the MSX, WISE, and *Spitzer* sources, respectively. Several sources were found to qualify the above criteria, which are listed in Table 4. The table presents the designation of the sources, their coordinates, flux densities, information concerning the type of the protostellar object, matching with another source in the table, and coincidence with a molecular or IR structure.

Among the MSX sources we found one MYSO candidate, which coincides with the center of IRAS 12326-6245, and one CHII region candidate, which coincides with a WISE Class II candidate (see below). Before attempting to identify the candidate YSOs from the listed WISE and *Spitzer* sources, we selected the non-YSO sources with excess infrared emission, such as PAH-emitting galaxies, broad-line active galactic nuclei (AGNs), unresolved knots of shock emission, and PAH-emission features. Then, a total of 89 and 51 WISE and *Spitzer* sources, respectively, were dropped from the lists. Among the remaining 311 WISE and 759 *Spitzer* sources, 12 (5 WISE and 7 *Spitzer*) were identified as Class I sources (i.e. sources with IR emission arising mainly from a dense infalling envelope, including flat spectrum objects) and 60 (43 WISE and 17 *Spitzer*) as Class II sources (i.e. pre-MS stars with optically thick disks).

The location of the identified candidate YSOs is shown in Fig. 8, where the 8.0 and 5.8 $\mu$m emissions together with the emission of both the $^{13}$CO and CO structures (i.e, Component A and Features 1, 2 and 3) are also displayed. As expected, the bulk of the candidate YSOs are seen projected onto the densest molecular gas (Component A). A noticeable feature is the concentration of sources along the two brightest PDR areas which, as mentioned in Sect. 3.2, delineates the borders of the molecular condensations. Namely, the WISE sources #5, #23, #24, #25, #27, #28, #29, #30, #32, and #35 to #47, seem to be related to the PDR closer to the ionized gas bordering the molecular emission of MC3 and MC4 (noted as (+) in the last column of Table 4), while WISE sources #7, #18, #19, #20, #21, #22, and #26, and *Spitzer* sources #54, #65, #67, #68, and #69 lie along the PDR that lies farther away from the ionized gas and related to the densest parts of MC3, MC4, and MC5 (noted as (*) in Table 4). Not surprisingly, another appreciable concentration of candidate YSOs, namely WISE sources #3, #6, #10, #11, #12, and #13, *Spitzer* sources #58, #59, #60, #66, and #71, and MSX sources #1 and #2 can be noticed in the region of the molecular concentration MC3.

### 5.3. The source IRAS 12326-6245

As shown in Figs. 1 and 4 the source IRAS 12326-6245 is very bright in the continuum emission at 870 $\mu$m (no emission at this wavelength is detected above the 3 rms limit outside the IRAS source). The emission at 870 $\mu$m is usually optically thin and dominated by the thermal emission from dust contained in dense material (e.g. dense molecular cores or filaments). Then, we used the image of ATLASGAL to more confidently derive the beam-averaged density using Eq. 12. For the calculations we adopted $\kappa_{870}$ = 1.85 cm$^2$ g$^{-1}$, a value representative for relatively dense molecular clouds (Ossenkopf & Henning 1994; Henning et al. 1995) and $T_{\rm dust}$ = 30 K (see Sect. 3.4) and we obtained a column density $N(H_2)$=8.2 × $10^{23}$ cm$^{-2}$. This value is some higher than those derived for MC3 in Sect. 3.2 from the $^{13}$CO(2-1) and C$^{18}$O(2-1) emissions (~ 1 × $10^{23}$ cm$^{-2}$). We keep in mid, however, that the column density values derived from continuum IR and carbon monoxide emissions are strongly dependant of the adopted abundances (dust and carbon monoxide-to $H_2$).

As mentioned in Sect. 2, we used the high-density tracer lines HCN(3-2) and HCO$^+$(3-2) tu study in more detail the molecular gas of IRAS 12326-6245. The emission of these lines in the velocity intervals from −47.6 to −29.2 km s$^{-1}$ and −44.8

**Table 4.** YSO candidates obtained from MSX, WISE, and *Spitzer* catalogues.

| **MSX sources** | | | | | | | | |
|---|---|---|---|---|---|---|---|---|
| # | Designation | $\alpha$ [h m s] | $\delta$ [° ′ ″] | $F_8$ [Jy] | $F_{12}$ [Jy] | $F_{14}$ [Jy] | $F_{21}$ [Jy] | Notes (class, match with other YSO and with $^{13}$CO/CO or IR structure) |
| 1 | G301.1364-00.2249 | 12 35 35.2 | –63 02 30 | 1.41 | 5.30 | 17.92 | 120.23 | (MYSO) MC3, WISE #6 |
| 2 | G301.1300-00.2354 | 12 35 31.5 | –63 03 06 | 2.216 | 2.702 | 1.477 | 8.930 | (CHII) MC3, WISE #3 |
| **WISE sources** | | | | | | | | |
| # | Designation | $\alpha$ [h m s] | $\delta$ [° ′ ″] | W1 [mag] | W2 [mag] | W3 [mag] | W4 [mag] | |
| 3 | J123531.48-630306.4 | 12 35 31.5 | –63 03 06.4 | 8.759 | 7.615 | 3.207 | -0.535 | (Class I), MC3, MSX #2 |
| 4 | J123529.88-630417.1 | 12 35 29.9 | –63 04 17.1 | 11.847 | 10.812 | 5.958 | 2.858 | (Class I), MC2 |
| 5 | J123553.78-630012.6 | 12 35 53.8 | –63 00 12.6 | 9.87 | 8.769 | 5.207 | 1.367 | (Class I), (+) |
| 6 | J123535.13-630230.3 | 12 35 35.1 | –63 02 30.3 | 9.49 | 6.629 | 1.011 | -3.604 | (Class I), MC3, MSX #1 |
| 7 | J123534.52-630147.8 | 12 35 34.5 | –63 01 47.8 | 11.804 | 10.715 | 5.25 | 2.989 | (Class I), MC3, (*) |
| 8 | J123529.71-630425.9 | 12 35 29.7 | –63 04 25.9 | 10.829 | 9.987 | 6.386 | 4.376 | (Class II), MC2 |
| 9 | J123528.94-630432.6 | 12 35 28.9 | –63 04 32.6 | 10.492 | 9.912 | 6.113 | 3.56 | (Class II), MC2 |
| 10 | J123531.19-630328.3 | 12 35 31.2 | –63 03 28.3 | 10.324 | 9.984 | 6.269 | 3.648 | (Class II), MC3 |
| 11 | J123538.44-630318.5 | 12 35 38.5 | –63 03 18.5 | 13.115 | 12.557 | 6.902 | 3.138 | (Class II), MC3 |
| 12 | J123537.22-630300.1 | 12 35 37.2 | –63 03 00.1 | 11.906 | 10.999 | 8.069 | 1.563 | (Class II), MC3 |
| 13 | J123534.55-630311.1 | 12 35 34.6 | –63 03 11.1 | 11.405 | 10.717 | 5.906 | 3.999 | (Class II), MC3 |
| 14 | J123628.80-630500.5 | 12 36 28.8 | –63 05 00.5 | 10.379 | 9.698 | 6.464 | 4.797 | (Class II), Feature 2, *Spitzer* #61 |
| 15 | J123606.78-630458.5 | 12 36 06.8 | –63 04 58.5 | 10.812 | 10.396 | 9.114 | 6.107 | (Class II) |
| 16 | J123553.95-625717.3 | 12 35 53.9 | - -62 57 17.3 | 12.834 | 12.427 | 5.898 | 3.722 | (Class II) |
| 17 | J123556.74-625804.3 | 12 35 56.7 | –62 58 04.3 | 13.196 | 12.637 | 6.007 | 4.376 | (Class II) |
| 18 | J123556.58-630058.1 | 12 35 56.6 | –63 00 58.1 | 12.681 | 12.309 | 6.877 | 5.598 | (Class II), MC5, (*) |
| 19 | J123559.25-630043.5 | 12 35 59.3 | –63 00 43.5 | 12.784 | 12.065 | 6.416 | 4.826 | (Class II), MC5, (*) |
| 20 | J123605.26-630000.2 | 12 36 05.3 | –63 00 00.2 | 12.44 | 11.992 | 7.689 | 5.894 | (Class II), MC5, (*) |
| 21 | J123608.20-625952.4 | 12 36 08.2 | –62 59 52.4 | 13.621 | 12.973 | 7.051 | 5.06 | (Class II), MC5, (*) |
| 22 | J123544.39-630151.3 | 12 35 44.4 | –63 01 51.3 | 12.362 | 11.598 | 7.181 | 4.462 | (Class II), MC3, (*) |
| 23 | J123535.61-630129.4 | 12 35 35.6 | –63 01 29.4 | 11.64 | 11.000 | 5.101 | 3.019 | (Class II), MC3, (+) |
| 24 | J123533.44-630130.5 | 12 35 33.4 | –63 01 30.5 | 11.504 | 10.981 | 5.308 | 2.927 | (Class II), MC3, (+) |
| 25 | J123539.82-630127.8 | 12 35 39.8 | –63 01 27.8 | 11.651 | 11.14 | 6.441 | 3.786 | (Class II), MC3, (+) |
| 26 | J123542.44-630148.3 | 12 35 42.3 | –63 01 48.3 | 11.042 | 10.237 | 6.363 | 2.654 | (Class II), MC3, (*), *Spitzer* #67 |
| 27 | J123538.39-630139.4 | 12 35 38.4 | –63 01 39.4 | 10.882 | 10.354 | 5.752 | 2.963 | (Class II), MC3, (+) |
| 28 | J123525.27-630114.3 | 12 35 25.3 | –63 01 14.3 | 9.593 | 8.952 | 4.275 | 2.262 | (Class II), MC3, (+) |
| 29 | J123528.77-630113.8 | 12 35 28.8 | –63 01 13.8 | 10.472 | 9.535 | 4.4 | 2.781 | (Class II), MC3, (+) |
| 30 | J123522.97-630048.0 | 12 35 23.0 | –63 00 48.0 | 11.545 | 10.94 | 6.364 | 1.844 | (Class II), (+) |
| 31 | J123526.73-630156.8 | 12 35 26.7 | –63 01 56.8 | 11.679 | 10.821 | 5.627 | 2.865 | (Class II), MC3 |
| 32 | J123521.24-630158.0 | 12 35 21.2 | –63 01 58.0 | 11.983 | 11.316 | 5.168 | 2.302 | (Class II), MC3, (+) |
| 33 | J123525.41-630204.4 | 12 35 25.4 | –63 02 04.4 | 11.457 | 10.729 | 5.582 | 3.669 | (Class II), MC3 |
| 34 | J123524.65-630218.0 | 12 35 24.7 | –63 02 18.0 | 11.548 | 10.785 | 5.839 | 3.296 | (Class II), MC3 |
| 35 | J123525.28-630126.8 | 12 35 25.3 | –63 01 26.8 | 10.764 | 10.072 | 5.26 | 4.748 | (Class II), MC3, (+) |
| 36 | J123552.92-625938.6 | 12 35 52.9 | –62 59 38.6 | 13.013 | 12.391 | 6.458 | 4.429 | (Class II), (+) |
| 37 | J123546.50-630010.4 | 12 35 46.5 | –63 00 10.4 | 13.483 | 12.56 | 6.118 | 4.25 | (Class II), (+) |
| 38 | J123551.36-630013.5 | 12 35 51.4 | –63 00 13.5 | 12.246 | 11.293 | 5.803 | 4.145 | (Class II), (+) |
| 39 | J123550.35-630001.0 | 12 35 50.4 | –63 00 01.0 | 12.141 | 11.6 | 6.098 | 4.645 | (Class II), (+) |
| 40 | J123541.99-630100.8 | 12 35 42.0 | –63 01 00.8 | 11.681 | 10.913 | 4.941 | 3.329 | (Class II), (+) |
| 41 | J123543.50-630002.3 | 12 35 43.5 | –63 00 02.3 | 13.039 | 12.656 | 7.897 | 4.866 | (Class II), (+) |
| 42 | J123543.44-630013.6 | 12 35 43.4 | –63 00 13.6 | 12.344 | 12.003 | 6.657 | 4.019 | (Class II), (+) |
| 43 | J123542.11-630037.9 | 12 35 42.1 | –63 00 37.9 | 12.257 | 11.573 | 5.277 | 3.368 | (Class II), (+) |
| 44 | J123543.69-630050.6 | 12 35 43.7 | –63 00 50.6 | 11.771 | 11.174 | 5.177 | 3.43 | (Class II), (+) |
| 45 | J123545.43-630023.2 | 12 35 45.4 | –63 00 23.2 | 11.848 | 11.265 | 5.344 | 3.169 | (Class II), (+) |
| 46 | J123544.72-630038.4 | 12 35 44.7 | –63 00 38.4 | 12.206 | 11.608 | 5.446 | 4.213 | (Class II), (+) |
| 47 | J123543.60-630027.6 | 12 35 43.6 | –63 00 27.6 | 12.647 | 12.25 | 6.496 | 5.909 | (Class II), (+) |
| 48 | J123544.53-625720.1 | 12 35 44.5 | –62 57 20.1 | 7.801 | 6.65 | 5.019 | 4.336 | (Class II), *Spitzer* #52 |
| 49 | J123454.60-630009.5 | 12 34 54.6 | –63 00 09.5 | 11.662 | 11.15 | 8.66 | 6.146 | (Class II), Feature 3, *Spitzer* #72 |
| 50 | J123558.47-625603.9 | 12 35 58.5 | –62 56 03.9 | 10.983 | 10.688 | 7.725 | 5.376 | (Class II) |

to −32.5 km s$^{-1}$, respectively, are shown in Fig 9a and 9b. Their emissions show a good morphological correspondence with that at 870 $\mu$m (see Fig. 4) and seems to be delineating a region that appears obscured in the 8.0 and 5.8 $\mu$m emissions. They are, certainly, the HCN and HCO$^+$ counterparts of the molecular condensation MC3.

**Table 4.** Continued.

| *Spitzer* **sources** | | | | | | | | |
|---|---|---|---|---|---|---|---|---|
| # | Designation | $\alpha$ | $\delta$ | 3.6 $\mu$m | 4.5 $\mu$m | 5.8 $\mu$m | 8.0 $\mu$m | |
| | | [h m s] | [$\circ$ $\prime$ $\prime\prime$] | [mag] | [mag] | [mag] | [mag] | |
| 51 | G301.1340-00.0894 | 12 35 38.3 | –62 54 21.5 | 12.44 | 11.532 | 10.577 | 9.693 | (Class I) |
| 52 | G301.1489-00.1383 | 12 35 44.5 | –62 57 20.5 | 8.62 | 7.55 | 6.595 | 5.873 | (Class I), WISE #48 |
| 53 | G301.1866-00.1701 | 12 36 03.4 | –62 59 23.0 | 12.424 | 11.565 | 10.773 | 9.521 | (Class I) |
| 54 | G301.1955-00.2012 | 12 36 07.1 | –63 01 16.6 | 11.595 | 10.529 | 9.709 | 8.791 | (Class I), MC5, (*) |
| 55 | G301.1766-00.2110 | 12 35 56.8 | –63 01 47.8 | 14.545 | 12.909 | 11.945 | 12.002 | (Class I), MC4 |
| 56 | G301.2000-00.1534 | 12 36 11.0 | –62 58 25.8 | 13.885 | 12.788 | 11.921 | 10.916 | (Class I) |
| 57 | G301.1338-00.2711 | 12 35 32.2 | –63 05 14.4 | 12.721 | 11.54 | 10.612 | 9.959 | (Class I), MC1 |
| 58 | G301.1402-00.2298 | 12 35 37.0 | –63 02 47.4 | 12.521 | 11.843 | 11.118 | 10.65 | (Class II), MC3 |
| 59 | G301.1395-00.2303 | 12 35 36.6 | –63 02 49.0 | 11.273 | 10.604 | 10.012 | 9.482 | (Class II), MC3 |
| 60 | G301.1523-00.2264 | 12 35 43.5 | –63 02 37.8 | 12.498 | 12.146 | 11.893 | 10.887 | (Class II), MC3 |
| 61 | G301.2400-00.2609 | 12 36 28.8 | –63 05 00.6 | 10.204 | 9.729 | 9.231 | 7.869 | (Class II), Feature 2, WISE #14 |
| 62 | G301.1973-00.2637 | 12 36 06.1 | –63 05 01.6 | 11.215 | 10.808 | 10.571 | 10.131 | (Class II) |
| 63 | G301.2169-00.2211 | 12 36 17.8 | –63 02 32.7 | 13.615 | 12.915 | 12.217 | 11.599 | (Class II), MC6 |
| 64 | G301.1745-00.2102 | 12 35 55.7 | –63 01 44.5 | 13.464 | 12.670 | 12.148 | 10.998 | (Class II) |
| 65 | G301.2153-00.1838 | 12 36 18.1 | –63 00 18.3 | 7.683 | 7.482 | 7.007 | 6.772 | (Class II), MC5, (*) |
| 66 | G301.1311-00.2271 | 12 35 32.3 | –63 02 35.7 | 12.992 | 11.898 | 11.354 | 10.504 | (Class II), MC3 |
| 67 | G301.1500-00.2124 | 12 35 42.7 | –63 01 47.0 | 11.332 | 10.95 | 10.353 | 9.342 | (Class II), MC3, (*), WISE #26 |
| 68 | G301.1402-00.2155 | 12 35 37.5 | –63 01 56.0 | 11.273 | 10.637 | 10.065 | 9.522 | (Class II), MC3, (*) |
| 69 | G301.1432-00.2154 | 12 35 39.9 | –63 01 56.3 | 12.104 | 11.591 | 11.068 | 10.594 | (Class II), MC3, (*) |
| 70 | G301.1090-00.1906 | 12 35 21.8 | –63 00 19.6 | 13.625 | 12.923 | 12.308 | 11.642 | (Class II) |
| 71 | G301.1250-00.2201 | 12 35 29.3 | –63 02 09.2 | 10.166 | 9.538 | 8.947 | 8.425 | (Class II), MC3 |
| 72 | G301.0569-00.1911 | 12 34 54.3 | –63 00 09.5 | 12.334 | 11.901 | 11.645 | 10.713 | (Class II), Feature 3 |
| 73 | G301.0578-00.1910 | 12 34 54.8 | –63 00 09.4 | 12.095 | 11.671 | 11.336 | 10.556 | (Class II), Feature 3, WISE #49 |
| 74 | G301.1525-00.0712 | 12 35 48.6 | –62 53 20.2 | 12.940 | 12.224 | 11.714 | 11.15 | (Class II) |

Usually, excitation temperatures and column densities can be fitted from rotational diagrams containing multiple transitions of a given species (Goldsmith & Langer 1999). As a different approach, when only one or few spectral lines are available, LTE models can be numerically approximated using algorithms as the Markov chain Monte Carlo (MCMC). As a result, lines in LTE were simulated and compared with the observations (e.g. Mackay 2003; Comito et al. 2005; Maret et al. 2011; Foreman-Mackey et al. 2013; Möller et al. 2017).

The results presented here are compatible to those obtained by Dedes et al. (2011) in IRAS 12326-6245 who used LTE models to derive beam-averaged column densities using species which exhibited only one or two lines. They adopted excitation temperatures of 150 K and 50 K to represent the excitation conditions of a seeming hot core region and extended envelope, respectively. In order to simulate the spectral lines reported here, we tested those assumptions in our calculations. Hence, we computed LTE-MCMC solutions adopting as free and fixed parameters the column density and temperature, respectively. Considering that routines take as input the observed lines, the solutions that we presented are those obtained from the averaged spectra considering the different offsets, since the individual solutions for each one of them were similar. That also is a consequence of the homogeneous emission traced by the species analyzed here. In Fig. 9 we show the average spectra (in antenna temperature) of HCN(3-2) and $HCO^+$(3-2). For the sake of the analysis, we also included the optically thin lines of $^{13}$CO(2-1) and C$^{18}$O(2-1) in the study.

From a simple LTE model of the $^{13}$CO(2-1) line, adopting excitation temperatures and column densities as free parameters, we obtained $T_{\rm exc}$ = 52 ± 5 K and $N(^{13}{\rm CO}) = (2.1 \pm 0.1) \times 10^{17}$ cm$^{-2}$. An alternative solution was obtained assuming $T_{\rm exc}$ = 50 K, that yielded approximately the same column density, $N(^{13}{\rm CO}) \simeq 2 \times 10^{17}$ cm$^{-2}$ (see Fig. 9c). Adopting an abundance CO/$^{13}$CO ~ 62 (Langer & Penzias 1993), this implies a column density $N({\rm CO}) \simeq 1.2 \times 10^{19}$ cm$^{-2}$. This value is relatively in good agreement with that obtained by Dedes et al. (2011), who estimated $N({\rm CO})=2.8 \times 10^{19}$ cm$^{-2}$ with $T$=50 K from models including isotopologues and isotopic ratios (e.g. $^{12}$C/$^{13}$C = 60, $^{16}$O/$^{17}$O = 1500). Fig. 9d exhibits the convergence of solutions through a corner diagram, which shows the distribution of values for both free parameters. Column densities of C$^{18}$O(2-1) and $HCO^+$(3-2) were derived assuming $T_{\rm exc}$=50 K, yielding to $N({\rm C^{18}O}) = (3.9 \pm 0.1) \times 10^{16}$ cm$^{-2}$ (Fig. 9d) and $N(HCO^+) = (5.2 \pm 0.1) \times 10^{13}$ cm$^{-2}$ (Fig. 9b), respectively.

For the case of the HCN(3-2) line, LTE models using the column density and excitation temperature as free parameters yielded $N({\rm HCN}) = (1.9 \pm 0.3) \times 10^{14}$ cm$^{-2}$ and $T_{\rm exc}$=156± 30 K. This is also in line with Dedes et al. (2011) who derived for DCN a column density of $3 \times 10^{13}$ cm$^{-2}$ from models assuming a fixed temperature value of $T$=150 K. From a model with the fixed value $T_{\rm exc}$=150 K, a similar column density was obtained ($N({\rm HCN}) \simeq 1.9 \times 10^{14}$ cm$^{-2}$; see Fig. 9a). Then, from the different models, it seems that the HCN temperatures can be given by a vast distribution of values which are around 150 K. In comparison with the DCN column density derived by Dedes et al. (2011), an HCN/DCN ratio would be around 6, nonetheless such ratio should be interpreted as a rough approximation. Concerning uncertainties, the results presented here are approximations that should be considered (at least) within the calibration uncertainty, since several assumptions were adopted for single transitions. In order to inspect the quality of the fits, in Fig. 9 we also exhibit the residuals after subtracting the emission lines from their LTE models.

Broadly, considering the good match between observations and models (e.g. Roueff et al. 2020), the conditions above and

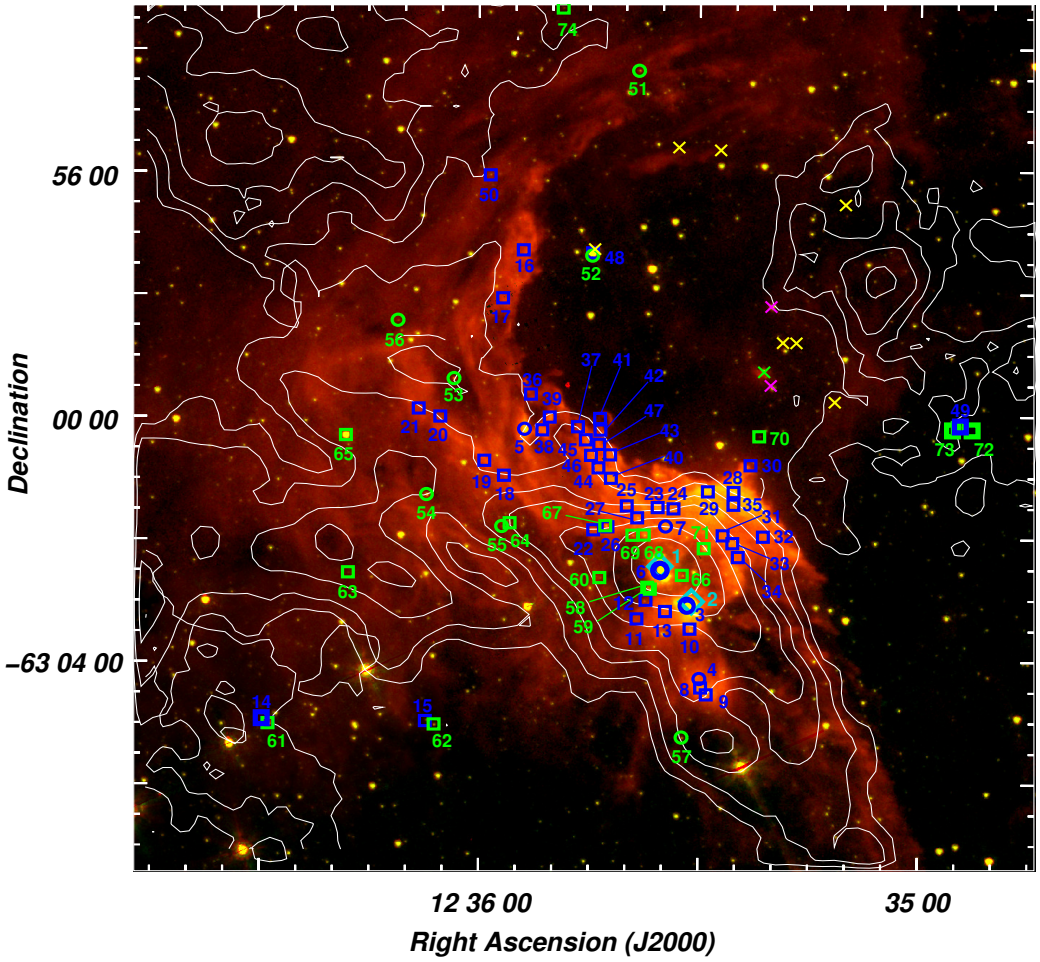


**Fig. 8.** MSX, WISE and *Spitzer* candidate YSOs projected onto the IRAC-Glimpse image at 8.0 and 5.8 $\mu$m. Cyan diamonds indicate the MSX sources, blue circles and blue squares indicate WISE Class I and Class II sources, respectively, and green circles and green squares indicate the *Spitzer* Class I and Class II sources, respectively. Numerical references of YSOs are based on those from Table 4. The size of the symbols do not necessary match the angular size of the sources. Ionizing candidate stars identified in Sect 5.1 are also indicated by crosses in magenta (O9V), green (B1V), and yellow (B2V or later). White contours indicate the $^{13}$CO emission of Component A (first contour level ~ 8 rms) and the CO emission of Feature 1 (first contour level ~13 rms) , Feature 2 (first contour level ~12 rms), and Feature 3 (first contour level ~10 rms).

LTE hypotheses seem to be appropriate for the scenario proposed by Dedes et al. (2011) for IRAS 12326-6245, with a two-temperature regime of ~ 150 K and 50 K, very likely corresponding to a hot core and an extended envelope, respectively.

## 6. Discussion

### 6.1. A model for S169 and its molecular environment

Since IR bubbles are believed to be born within dense molecular clouds, the classical scenario predicts that, in a uniform medium, the molecular gas around the bubble should expand spherically. Under that assumption, a molecular shell with a central velocity $V_0$ and an expansion velocity $V_{exp}$ should depict in a position-position diagram a 'disk-ring' pattern when observed at different velocities. At $V_0$ (corresponding to the systemic velocity of the bubble) the shell should attain its maximum diameter, while at extreme velocities (either negative or positive with respect to $V_0$) the molecular emission should resemble a disk. At intermediate velocities, the radius of the ring shrinks as the extreme velocity is approached. Although these features are rarely observed all together in the molecular gas around IR bubbles, the behaviour of the molecular gas around S169 certainly clashes with the classical IR bubble model.

In order to address the observed characteristics of the molecular gas associated with S169, we present a simple model taking into account its morphology, relative position with respect to the IR and H$\alpha$ emissions, and velocity intervals as constrains. Needless to say, we will assume that Component A, Feature 1, Feature 2, and Feature 3 are physically associated with S169, a well-grounded conclusion given their excellent morphological correspondence with the IR nebula. Hence, we propose that Component A and Features 1, 2, and 3 could be explained as an expanding partially complete semi-spherical structure. A simple sketch is presented in Fig. 10, where the Right Ascension axis is indicated for the sake of clarity (the Declination axis is then perpendicular to the sketch, increasing to the reader). The expansion of the molecular gas is then revealed by the velocity of the different molecular structures. The molecular gas approaching to Earth is depicted by the molecular structure at more negative velocity (Component A) with an approaching velocity $V_{appr} \approx -39$ km s$^{-1}$, while the molecular gas receding is depicted by the structure at more positive velocity (Feature 3) with a receding velocity $V_{rec} \approx -17$ km s$^{-1}$. Molecular structures at intermedi-

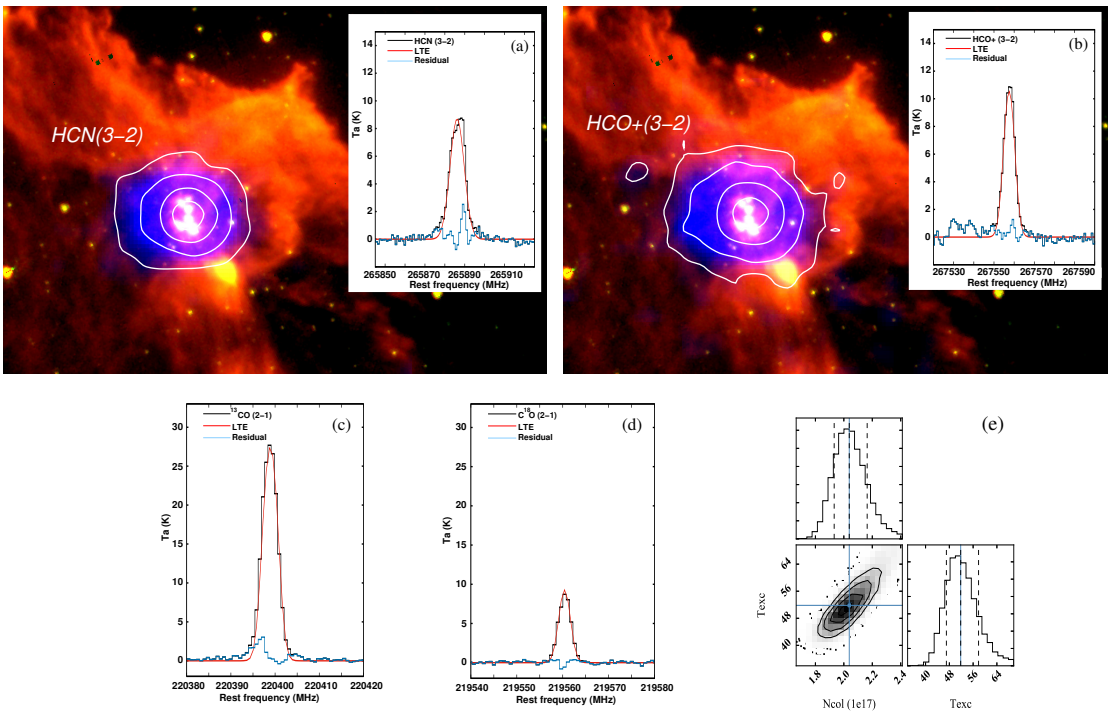


**Fig. 9.** *a)* to *d)* Average spectra from different offsets and LTE models for the molecular lines observed in the direction to IRAS 12326-6245. *a)* Spectral line and LTE model of the HCN(3-2) line. The synthetic spectrum, exhibited by the red dotted line, was obtained from LTE-MCMC calculations of the column density assuming $T_{\rm exc}$=150 K (see text), with a resultant density $N$=(1.9 ± 0.5) × $10^{14}$ cm$^{-2}$. The blue dotted line indicates the residual obtained from the subtraction between the observation and LTE model. In colors: Spatial distribution of the HCN(3-2) emission in the velocity interval from −47.6 to −29.2 km s$^{-1}$(color blue and white contours) superimposed on the IRAC 8 and 5.8 $\mu$m emissions (red and green colors). *b)* Spectral line and LTE model of the $HCO^+$(3-2) line and the synthetic spectrum obtained from LTE-MCMC calculations assuming $T_{\rm exc}$=50 K (see text), with a resultant density $N$=(5.2 ± 0.1) × $10^{13}$ cm$^{-2}$. In color: $HCO^+$(3-2) emission distribution in the velocity interval from −44.8 to −32.5 km s$^{-1}$ superimposed on the IRAC 8 and 5.8 $\mu$m emissions. The contour levels for HCN(3-2) are 0.25 (∼5 rms), 0.85, 2.2, and 4.0 K km s$^{-1}$, and for the $HCO^+$(3-2) line are 0.28 (∼ 5 rms), 0.8, 2.4, and 5 K km s$^{-1}$. *c)* $^{13}$CO(2-1) line and synthetic spectrum (red dashed line) obtained from LTE/MCMC calculations with resultant parameters $N$ = (2.1 ± 0.1) × $10^{17}$ cm$^{-2}$ and $T_{\rm exc}$ = 52 ± 5 K. *d)* Idem for the C$^{18}$O(2-1) with the synthetic spectrum obtained assuming $T_{\rm exc}$=50 K and a resultant density $N$=(3.9 ± 0.1) × $10^{16}$ cm$^{-2}$. *e)* Corner diagram of $^{13}$CO(2-1) displaying LTE solutions computed through the MCMC method. The column density and excitation temperature, labeled in the plot as Ncol (cm$^{-2}$) and Texc (K), respectively, were computed as free parameters. The resultant solution yielded Ncol = (2.1 ± 0.1) × $10^{17}$ cm$^{-2}$ and Texc = 52 ± 5 K. The corner diagram exhibits the 2D projection considering the distributions of each free parameter.

ate velocities (Features 1 and 2) represent then the molecular gas at $V_0 \approx -25$ km s$^{-1}$ expanding approximately in perpendicular directions with respect the direction to Earth, that is with expansion velocities with no (or small) components in the radial direction. A glance at Fig. 5 suggests that the expansion velocity of Features 1 and 2 might have components in the direction of the Declination axis, positive for the case of Feature 1 and negative for the case of Feature 2 (this cannot be depicted in the two-dimension sketch presented in Fig. 10).

Therefore, with this simple model we are able to explain not only the morphology and kinematics of the molecular gas, but also the characteristics of the ionized gas (traced by the radio continuum emission), which seems to be expanding against the molecular gas towards the east, north, and south, while it is expanding freely to the west, probably in a sort of a champagne-flow effect.

According to the model, a rough estimation of the expansion velocity of the molecular gas around S169 could be simply obtained by

$$V_{\rm exp} = \frac{|V_{\rm appr}| - |V_{\rm rec}|}{2 \times \cos(\theta)} \qquad (16)$$

being $\theta$ the angle between the line of sight and the direction of $V_{\rm exp}$ of Component A and Feature 2. Based on the morphology of the IR nebula, a conservative value $\theta$=25° can be adopted, and the obtained expansion velocity turns out to be $V_{\rm exp} \sim 12$ km s$^{-1}$. Having the expansion velocity, the dynamical age of the nebula, $t_{\rm dyn}$, can be derived considering a radius of 2.3±0.8 pc (∼ 4′ at a distance of $2.03^{+0.77}_{-0.61}$ kpc), which turns out to be in the range (1.2 - 2.6) × $10^5$ yr.

### 6.2. Distance to S169 and IRAS 12326-6245

As mentioned in Sect. 1 the adopted distance in the literature for IRAS 12326-6245 is 4.4 kpc. This value was first estimated by Osterloh et al. (1997) who performed a study of a number of southern IRAS sources using IR continuum and millimeter line data. The authors adopted distances that were taken from the literature where possible (either directly or by kinematic and spatial association with another source of known distance). Otherwise, kinematical distances were determined using the central velocity of the CS(2-1) or CO(2-1) emission lines and the Galactic rotation curve of Clemens (1985). For the case of IRAS 12326-6245 a kinematical distance could not be determined by the authors since the central velocity of the CS and CO lines (−39.4 km s$^{-1}$ and −39.7 km s$^{-1}$, respectively) are forbidden according to the Galactic rotation model. Then, the au-

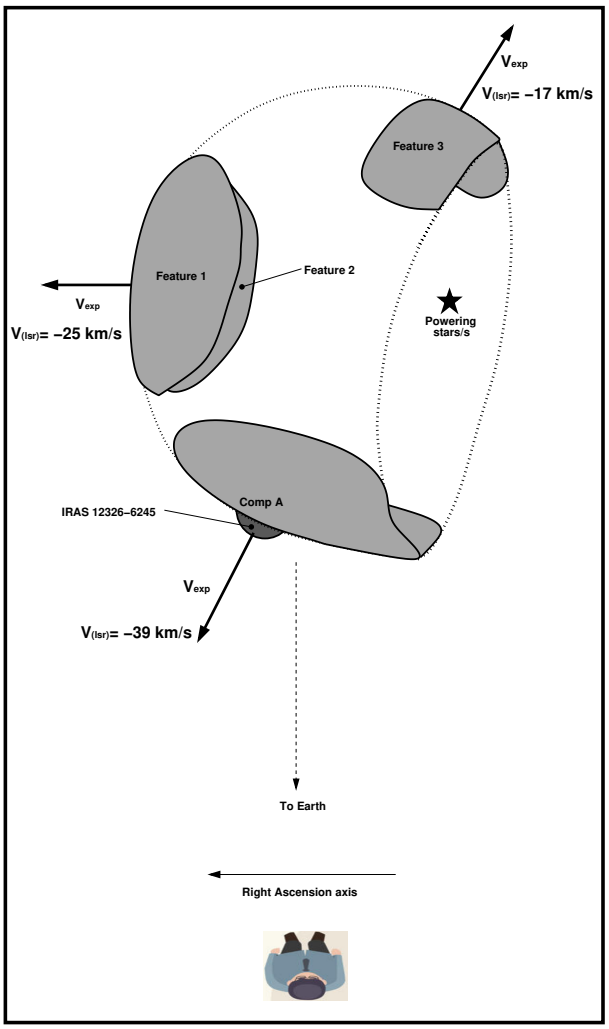


**Fig. 10.** Simple sketch of the proposed model to explain the morphology and velocity of the molecular gas associated with S169. The Right Ascension axis, as visualized by the observer, is indicated (the Declination axis is perpendicular to the plane of the sketch, increasing to the reader)

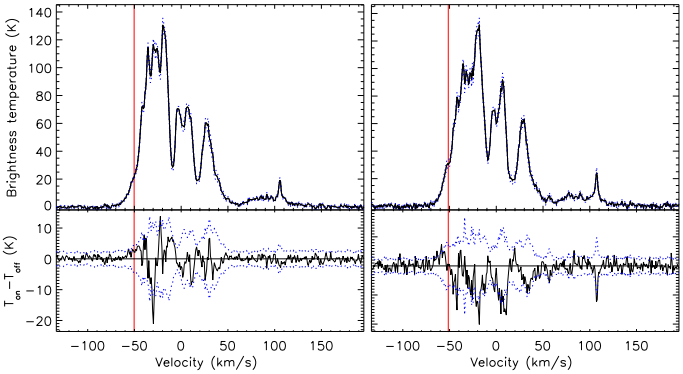


**Fig. 11.** *Left panel.* HI emission/absorption profile towards the bright southern component of the radio continuum arc-like feature. *Right panel.* Same for the extragalactic source at the north of the nebula. The error envelopes are plotted with blue dotted lines. Vertical red lines indicate the velocity of the tangent point.

thors adopted for IRAS 12326-6245 the distance to the source IRAS 1283-6128 (4.4 kpc) which is kinematically close to within 0.5 km s$^{-1}$, and spatially to within 2°.

In Sect. 3.1 we confirmed the physical association between S169 and IRAS 12326-6245. Further, according to the model proposed in Sect. 6.1, the source IRAS 12326-6245 (embedded in Comp A), is expanding at a velocity coarsely estimated as $V_{exp} \sim 12$ km s$^{-1}$ with respect to the systemic velocity of the bubble ($V_0 \approx -25$ km s$^{-1}$). Assuming that our model is well-suited to explain the characteristics of the molecular gas around the bubble nebula, this leads to the unavoidable conclusion that the velocity reported in the literature for IRAS 12326-6245 ($\sim -39$ km s$^{-1}$) does not represent the velocity of the ISM in the surroundings of both, the IRAS source and S169. This is understandable considering that previous studies of IRAS 12326-6245 were not performed in the whole context of the nebula S169, but rather focused only on the IRAS source. Instead, we believe that the velocity of Features 1 and 2 ($\sim -25$ km s$^{-1}$), corresponding approximately to the systemic velocity of the bubble nebula, is more suitable for determining the kinematical distance for both, S169 and IRAS 12326-6245. Furthermore, in a study of the rotation curve in the Southern Galaxy, Alvarez et al. (1990) have found an excess anomally of +12.2 km s$^{-1}$ in the terminal velocities in the Galactic longitude range between $l$ = 280 and $l$ = 312, with respect to the trend in the rest of the IV Galactic quadrant. This excess includes the region studied here, since our source is at Galactic coordinates ($l, b$) = (301.134, –0.225). Then adopting a velocity of −25 km s$^{-1}$, using the rotation curve of Reid et al. (2014) with the Monte Carlo method[13] (see Wenger et al. 2018 for details), and a conservative velocity uncertainty of 1 km s$^{-1}$, two kinematical distances are obtained, namely a near-kinematical distance of $2.03^{+0.77}_{-0.61}$ kpc, and a far-kinematical distance of $6.59^{+0.62}_{-0.77}$ kpc.

To resolve the twofold ambiguity in kinematic distance we made use of the HI data from the SGPS constructing absorption profiles towards the bright southern component of the radio continuum arc-like feature and, for comparison, towards the extragalactic source. The radio continuum data were convolved to a beam of 2 arcmin to make them compatible with the resolution of the HI data. The expected off-source profile was computed using a bilinear interpolation method as described in Reynoso et al. (2017). The results are shown in Fig. 11. From the emission spectra, the tangent point lies at $\sim -50$ km s$^{-1}$ (indicated with red vertical lines in Fig. 11), while emission at the outer Galaxy is observed as far as $\sim +110$ km s$^{-1}$. The extragalactic source (right panel) exhibits, as expected, absorption features up to $\sim -45$ km s$^{-1}$, coincident with the tangent point within a few km s$^{-1}$, a difference that can be ascribed to the ISM turbulence. Another clear absorption feature at $\sim +110$ km s$^{-1}$ confirms the extragalactic nature of this source. In contrast, the profile corresponding to the arc-like feature (left panel) displays the last significant absorption feature at about $\sim -30$ km s$^{-1}$. Considering the absence of absorption in a gap of about 20 km s$^{-1}$ between this velocity and the tangent point, it is very unlikely that S169 is located at the far side of the Solar circle. Based on these results, we conclude that the near kinematical distance ($2.03^{+0.77}_{-0.61}$ kpc) is the most adequate for S169. The detection of H$\alpha$ emission at the center of the nebula (see Fig.1), which is likely the optical counterpart of the ionized nebula, gives more support to this conclusion, since the absorption that could be produced by the ISM along the far kinematical distance ($\sim$ 6.6 kpc) would make the H$\alpha$ emission much fainter or even undetectable. Furthermore, the whole molecular cloud that contains IRAS 12326-6245 has

[13] https://www.treywenger.com/kd/index.php

been identified to be in the near side of the Carina Spiral Arm by Cohen et al. (1985).

### 6.3. Triggered star formation?

The spatial distribution of the candidate YSOs along the borders of the IR nebula and the densest part of the molecular gas (see Sect. 5.2) is indicative that triggered star forming process like collect-and-collapse (C&C; Elmegreen & Lada 1977) or radiative driven implosion (RDI; Lefloch & Lazareff 1994) might be acting on the nebula.

In order to test the C&C mechanism, we use the classical model of Whitworth et al. (1994) for expanding HII regions. Then, we estimated the fragmentation time, $t_{\rm frag}$, and the radius of the HII region when the fragmentation occurs, $R_{\rm frag}$, as

$$t_{\rm frag} = 1.56\, {a_{0.2}}^{7/11}\, n_3^{-5/11}\, (N_{49})^{-1/11}\ \ 10^6\ \ {\rm yr} \quad (17)$$

$$R_{\rm frag} = 5.8\, {a_{0.2}}^{4/11}\, n_3^{-6/11}\, (N_{49})^{1/11}\ \ {\rm pc} \quad (18)$$

being $a_{0.2}$ the isothermal sound speed in the compressed layer in units of 0.2 km s$^{-1}$ ($a_s$/0.2 km s$^{-1}$), $n_3$ the surrounding homogeneous infinite medium into which the HII region expands, in units of $10^3$ cm$^{-3}$ ($n_0/10^3$ cm$^{-3}$), and $N_{49}$ the number of ionizing Lyman continuum photons, in units of $10^{49}$ s$^{-1}$ ($N^*_{\rm Lyc}/10^{49}$ s$^{-1}$). We adopt $a_s$ = 0.2 km s$^{-1}$ for the collected layer (likely a lower limit since both turbulence and extra heating from intense sub-Lyman-continuum photons leaking from the HII region could increase this value) and $N^*_{\rm Lyc} = 2.5 \times 10^{47}$ s$^{-1}$ (see Sect.4). To estimate the initial density, $n_0$, we averaged the total mass of the molecular gas around S169 ($\sim (7.4 \pm 4.4) \times 10^3$ M$_\odot$) over a sphere of 2.3 ± 0.8 pc in radius, which yields a density in the range $n_0$ = (0.35 - 12) × $10^3$ cm$^{-3}$. Thus, we obtain $t_{\rm frag}$ in the range between 0.5 and 2.2 Myr and $R_{\rm frag}$ between 1.1 and 7.4 pc.

A comparison between $R_{\rm frag}$ and the present radius of the nebula suggests (within errors) that the C&C process may be acting in S169. On the contrary, the estimated fragmentation time is higher than the $t_{\rm dyn}$ derived for the region in Sect. 6.1. Then, there is no conclusive evidence to support that protostellar objects at the borders of S169 could have been formed as a result of the C&C mechanism. It should be kept in mind, however, that the model of Whitworth et al. (1994) is valid for evolution of the HII regions only in a uniform molecular environment, which is certainly not the case of S169.

As regards of the possibility that the RDI process is taking place in the region, a more detailed study, with better angular resolutions of both the molecular and radio continuum data, is necessary. Nevertheless, we can point out that the presence of the intense PDR emission detected as a bright rim of the densest molecular feature suggests that the RDI process could be responsible for the formation of the candidate YSOs located behind this border and, in particular, for the IR source IRAS 12326-6245.

## 7. Summary

As part of a project aimed at characterizing and studying the physical properties of Galactic IR bubbles and their surroundings, we present a multiwavelength analysis of the southern IR dust bubble S169 associated with the massive star forming core IRAS 12326-6245. To analize the characteristics of the molecular gas in the whole nebula we have used CO(2-1), $^{13}$CO(2-1), C$^{18}$O(2-1) line data, while for the IRAS source we also used HCN(3-2), and HCO$^+$(3-2) data, all obtained with the APEX telescope. To study the characteristics of the dust and ionized gas, as well as to investigate the presence of stellar and protostellar objects in the nebula, we have used archival public data.

The analysis of the CO(2-1), $^{13}$CO(2-1), and C$^{18}$O(2-1) data allows us to identify the molecular gas linked to the nebula. We report three molecular components at ∼ −39, −25, and −17 km s$^{-1}$ (Components A, B, and C) which are morphologically correlated with different regions of the IR nebula. The component at −39 km s$^{-1}$ (Component A) is associated to the brightest part of the IR nebula (at the southern region) and is the only one detected in $^{13}$CO(2-1) and C$^{18}$O(2-1) emissions. For this component we have identified six molecular condensations (namely MC1, MC2, MC3, MC4, MC5, and MC6) based on the $^{13}$CO and C$^{18}$O emissions. These condensations have masses between 4000 and 24000 M$_\odot$, and H$_2$ column densities between ∼ 6×$10^{21}$ and 1×$10^{23}$ cm$^{-2}$. The densest one (MC3) is the molecular counterpart of IRAS 12326-6245 which demonstrates the physical association between the nebula and the IRAS source. LTE analyses of CO(2-1), $^{13}$CO(2-1), HCO$^+$(3-2) and HCN(3-2) indicate for this condensation two different gas conditions with temperatures of ∼ 50 and 150 K. This is indicative of the existence of an internal hot core and extended envelope, as suggested by Dedes et al. (2011). For this condensation, an H$_2$ column density up to ∼ 8×$10^{23}$ cm$^{-2}$ is obtained from the emission at 870 $\mu$m.

The molecular components at −25 and −17 km s$^{-1}$ (Components B and C) seem to be associated with the faintest and more external regions of the IR nebula. Unlike Component A, Components B and C are not detected in $^{13}$CO and C$^{18}$O emissions, which indicates that they are composed by low density gas. This can be confirmed from *Herschel* images at 70, 160, and 350 $\mu$m.

With the purpose of explaining the spatial distribution and velocity of Component A, B, and C, a very simple model is proposed, which consists of a partially complete semi sphere-like structure expanding at ∼ 12 km s$^{-1}$. According to the model, Component A represents the molecular gas approaching at a velocity of −39 km s$^{-1}$ while Component C (Feature 3) the molecular gas receding at a velocity of −17 km s$^{-1}$. The systemic velocity of the molecular gas associated with the bubble is then −25 km s$^{-1}$, which is the velocity of Component B (Features 1 and 2). The distribution in the radio continuum emission at 843 MHz suggests an HII region bounded by ionization to the east, north and south, and by density to the west in a probable champagne-flow effect. This seems to be in line with the model proposed for the molecular gas. The model proposed for the molecular gas brings an additional discussion about the distance of IRAS 12326-6245 (and consequently S169) since the radial velocity adopted in the literature for the IRAS source (∼ –39 km s$^{-1}$) would not be representing the velocity of the ISM in its surroundings. Rather, we believe that the systemic velocity of the bubble (–25 km s$^{-1}$) is more adequate to determine its kinematical distance. Then, using the Galactic rotation model and HI absorption profiles we determined a kinematical distance of $2.03^{+0.77}_{-0.61}$ kpc for S169 and IRAS 12326-6245.

Using point source catalogs, we identified 10 ionizing stars candidates projected onto the cavity. They have spectral types between O9V and B2, which are necessary to sustain the current level of ionization of the HII region. We also identified a number of candidate YSOs projected mostly onto Component A, more precisely MC3, MC4, and MC5 , confirming that active star formation has developed in the borders of the bubble. After comparing the fragmentation time and fragmentation radius with the age and current radius of the nebula, we cannot assert that the C&C process is acting in the collected layers of gas at the edge of the bubble. We keep in mind, however, the limitations of the models applied to S169 and that other triggering star form-

ing process like RDI could also be active in pre-existing cores or bright-rimmed clouds at certain regions in the borders.

Summarizing, we found out that the infrared bubble S169 is a relatively young HII region which has profoundly affected its surroundings, creating a molecular shell that still posses a large expanding motion and where several condensations host candidate protostellar objects in their dense interiors, being the source IRAS 12326-6245 the most striking one.

*Acknowledgements.* N.U.D and M.A.C acknowledge support from UNLP, PPID G005 and CONICET grant PIP 112−201701−00507 (Argentina). L. B. acknowledges support from CONICYT project Basal. E.M. acknowledges support from the Brazilian agency CNPq (grant 150465/2019-0). L.A.S acknowledges support from UNLP PPID G005 grant. S.C., L.A.S. and E.M.R. are partially funded by CONICET grant PIP 112-201701-00604 (Argentina).

## References

Allen, L. E., Calvet, N., D'Alessio, P., et al. 2004, ApJS, 154, 363
Alvarez, H., May, J., & Bronfman, L. 1990, ApJ, 348, 495
Anderson, L. D., Deharveng, L., Zavagno, A., et al. 2015, ApJ, 800, 101
Anderson, L. D., Zavagno, A., Deharveng, L., et al. 2012, A&A, 542, A10
Araya, E., Hofner, P., Kurtz, S., Bronfman, L., & DeDeo, S. 2005, ApJS, 157, 279
Beichman, C. A., Neugebauer, G., Habing, H. J., Clegg, P. E., & Chester, T. J., eds. 1988, Infrared astronomical satellite (IRAS) catalogs and atlases. Volume 1: Explanatory supplement, Vol. 1
Benjamin, R. A., Churchwell, E., Babler, B. L., et al. 2003a, PASP, 115, 953
Benjamin, R. A., Churchwell, E., Babler, B. L., et al. 2003b, PASP, 115, 953
Bloemen, J. B. G. M., Strong, A. W., Mayer-Hasselwand er, H. A., et al. 1986, A&A, 154, 25
Bock, D. C. J., Large, M. I., & Sadler, E. M. 1999, AJ, 117, 1578
Borissova, J., Bonatto, C., Kurtev, R., et al. 2011, A&A, 532, A131
Bronfman, L., Nyman, L. A., & May, J. 1996, A&AS, 115, 81
Cappa, C. E., Duronea, N., Firpo, V., et al. 2016, A&A, 585, A30
Carpenter, J. M., Hillenbrand, L. A., & Skrutskie, M. F. 2001, AJ, 121, 3160
Caswell, J. L. 1998, MNRAS, 297, 215
Caswell, J. L. 2009, PASA, 26, 454
Chaisson, E. J. 1976, in Frontiers of Astrophysics, ed. E. H. Avrett, 259–351
Churchwell, E., Povich, M. S., Allen, D., et al. 2006, ApJ, 649, 759
Churchwell, E., Watson, D. F., Povich, M. S., et al. 2007, ApJ, 670, 428
Clemens, D. P. 1985, ApJ, 295, 422
Cohen, R. S., Grabelsky, D. A., May, J., et al. 1985, ApJ, 290, L15
Comito, C., Schilke, P., Phillips, T. G., et al. 2005, ApJS, 156, 127
Cousins, A. W. J. 1978, The Observatory, 98, 54
Dedes, C., Leurini, S., Wyrowski, F., et al. 2011, A&A, 526, A59
Deharveng, L., Lefloch, B., Kurtz, S., et al. 2008, A&A, 482, 585
Deharveng, L., Zavagno, A., Schuller, F., et al. 2009, A&A, 496, 177
Devine, K., Mori, J., Watson, C., Trujillo, L., & Hicks, M. 2018, ApJ, 861, 117
Digel, S. W., Grenier, I. A., Heithausen, A., Hunter, S. D., & Thaddeus, P. 1996, ApJ, 463, 609
Ducati, J. R., Bevilacqua, C. M., Rembold, S. r. B., & Ribeiro, D. 2001, ApJ, 558, 309
Duronea, N. U., Cappa, C. E., Bronfman, L., et al. 2017, A&A, 606, A8
Duronea, N. U., Vasquez, J., Gómez, L., et al. 2015, A&A, 582, A2
Egan, M. P., Price, S. D., & Kraemer, K. E. 2003, in Bulletin of the American Astronomical Society, Vol. 35, American Astronomical Society Meeting Abstracts, 1301
Elmegreen, B. G. & Lada, C. J. 1977, ApJ, 214, 725
Faúndez, S., Bronfman, L., Garay, G., et al. 2004, A&A, 426, 97
Figueira, M., Zavagno, A., Deharveng, L., et al. 2017, A&A, 600, A93
Foreman-Mackey, D., Hogg, D. W., Lang, D., & Goodman, J. 2013, PASP, 125, 306
Frerking, M. A., Langer, W. D., & Wilson, R. W. 1982, ApJ, 262, 590
Gaia Collaboration, Brown, A. G. A., Vallenari, A., et al. 2018, A&A, 616, A1
Gaia Collaboration, Prusti, T., de Bruijne, J. H. J., et al. 2016, A&A, 595, A1
Goldsmith, P. F. & Langer, W. D. 1999, ApJ, 517, 209
Güsten, R., Nyman, L. Å., Schilke, P., et al. 2006, A&A, 454, L13
Gutermuth, R. A., Megeath, S. T., Myers, P. C., et al. 2009, ApJS, 184, 18
Henden, A. A., Terrell, D., Welch, D., & Smith, T. C. 2010, in Bulletin of the American Astronomical Society, Vol. 42, American Astronomical Society Meeting Abstracts 215, 470.11
Henning, T., Lapinov, A., Schreyer, K., Stecklum, B., & Zinchenko, I. 2000, A&A, 364, 613
Henning, T., Michel, B., & Stognienko, R. 1995, Planet. Space Sci., 43, 1333
Hildebrand, R. H. 1983, QJRAS, 24, 267
Hill, T., Burton, M. G., Minier, V., et al. 2005, MNRAS, 363, 405
Hunter, S. D., Bertsch, D. L., Catelli, J. R., et al. 1997, ApJ, 481, 205
Inoue, A. K. 2001, AJ, 122, 1788
Junkes, N., Fuerst, E., & Reich, W. 1992, A&A, 261, 289
Kendrew, S., Beuther, H., Simpson, R., et al. 2016, ApJ, 825, 142
Kharchenko, N. V. & Roeser, S. 2009, VizieR Online Data Catalog, I/280B
Koenig, X. P., Leisawitz, D. T., Benford, D. J., et al. 2012, ApJ, 744, 130
Koornneef, J. 1983, A&A, 128, 84
Kurtz, S., Cesaroni, R., Churchwell, E., Hofner, P., & Walmsley, C. M. 2000, in Protostars and Planets IV, ed. V. Mannings, A. P. Boss, & S. S. Russell, 299–326
Langer, W. D. & Penzias, A. A. 1993, ApJ, 408, 539
Lefloch, B. & Lazareff, B. 1994, A&A, 289, 559
Liu, H.-L., Wu, Y., Li, J., et al. 2015, ApJ, 798, 30
Lumsden, S. L., Hoare, M. G., Oudmaijer, R. D., & Richards, D. 2002, MNRAS, 336, 621
Mackay, D. J. C. 2003, Information Theory, Inference and Learning Algorithms
MacLeod, G. C., Scalise, Eugenio, J., Saedt, S., Galt, J. A., & Gaylard, M. J. 1998, AJ, 116, 1897
Maret, S., Hily-Blant, P., Pety, J., Bardeau, S., & Reynier, E. 2011, A&A, 526, A47
Martins, F., Schaerer, D., & Hillier, D. J. 2005, A&A, 436, 1049
McClure-Griffiths, N. M., Dickey, J. M., Gaensler, B. M., et al. 2005, ApJS, 158, 178
Miettinen, O., Harju, J., Haikala, L. K., & Pomrén, C. 2006, A&A, 460, 721
Molinari, S., Swinyard, B., Bally, J., et al. 2010, A&A, 518, L100
Möller, T., Endres, C., & Schilke, P. 2017, A&A, 598, A7
Ossenkopf, V. & Henning, T. 1994, A&A, 291, 943
Osterloh, M., Henning, T., & Launhardt, R. 1997, ApJS, 110, 71
Panagia, N. & Walmsley, C. M. 1978, A&A, 70, 411
Parker, Q. A., Phillipps, S., Pierce, M. J., et al. 2005, MNRAS, 362, 689
Povich, M. S., Stone, J. M., Churchwell, E., et al. 2007, ApJ, 660, 346
Reid, M. J., Menten, K. M., Brunthaler, A., et al. 2014, ApJ, 783, 130
Reynoso, E. M., Cichowolski, S., & Walsh, A. J. 2017, MNRAS, 464, 3029
Rieke, G. H. & Lebofsky, M. J. 1985, ApJ, 288, 618
Rohlfs, K. & Wilson, T. L. 2004, Tools of radio astronomy
Roueff, A., Gerin, M., Gratier, P., et al. 2020, arXiv e-prints, arXiv:2005.08317
Samal, M. R., Zavagno, A., Deharveng, L., et al. 2014, A&A, 566, A122
Schmidt-Kaler. Th. 1982, In Landolt-Bornstein New Series, Group VI, Vol. 2b. (eds. K. Schaifers & H. H. Voigt), (Springer-Verlag, Berlin)
Schuller, F., Menten, K. M., Contreras, Y., et al. 2009, A&A, 504, 415
Skrutskie, M. F., Cutri, R. M., Stiening, R., et al. 2006, AJ, 131, 1163
Solomon, P. M., Rivolo, A. R., Barrett, J., & Yahil, A. 1987, ApJ, 319, 730
Strong, A. W. & Mattox, J. R. 1996, A&A, 308, L21
Tenorio-Tagle, G. 1979, A&A, 71, 59
Vassilev, V., Meledin, D., Lapkin, I., et al. 2008, A&A, 490, 1157
Watson, C., Povich, M. S., Churchwell, E. B., et al. 2008, ApJ, 681, 1341
Wenger, T. V., Balser, D. S., Anderson, L. D., & Bania, T. M. 2018, ApJ, 856, 52
Whitworth, A. P., Bhattal, A. S., Chapman, S. J., Disney, M. J., & Turner, J. A. 1994, MNRAS, 268, 291
Wright, E. L., Eisenhardt, P. R. M., Mainzer, A. K., et al. 2010, AJ, 140, 1868
Yamaguchi, R., Akira, M., & Yasuo, F. 1999, in Star Formation 1999, ed. T. Nakamoto, 383–384
Zavagno, A., Deharveng, L., Comerón, F., et al. 2006, A&A, 446, 171
Zinchenko, I., Henkel, C., & Mao, R. Q. 2000, A&A, 361, 1079